

# A two-part analysis of the Greenland Ice Sheet using glacial isostatic adjustment and bare ice albedo: from past and present to future

Master's Thesis

Raf Antwerpen

August 2020

---

---

## Abstract

Global sea level rise is a major present-day and future concern as it directly affects many people living in coastal communities. The Greenland Ice Sheet (GrIS) is currently the largest contributing ice sheet to global sea level rise, though it remains unclear, however, exactly how much sea level is going to rise and what role meltwater from the GrIS is going to play. To understand the behaviour of the GrIS in the future, we need to understand its behaviour both in the past and present. In this thesis I therefore focus on aspects of both the historic as well as the present-day contribution to sea level rise from the GrIS. The first chapter contains a study of the sensitivity of the GrIS to a historic warmer-than-present climate during the Holocene Thermal Maximum (HTM;  $\sim 11-5$  ka). During this period, especially Southwest Greenland was exposed to a warmer climate. In this study I focus on the extent of the ice margin in Southwest Greenland to increased temperatures during the HTM and what effect a changing ice margin has on the long-term viscoelastic response of the solid Earth underlying the southwestern region of the GrIS. By doing this, I infer what ongoing adjustments of the changing ice mass load since the Last Glacial Maximum (26.5-20 ka) are present in current sea level and geodetic signals in Southwest Greenland and how this affects our understanding of present-day ice melt from the GrIS. The second chapter contains a study of the present-day behaviour of the GrIS. In particular, the variability of the extent and albedo of the bare ice zone. Bare ice is responsible for the majority of meltwater production and runoff from the GrIS through its low albedo and absorption of solar radiation. Proper representation of the bare ice zone in climate models is thus imperative for accurately modeling future melt from the GrIS. In this study I focus on the representation of the bare ice extent and albedo variability on the GrIS in the Modèle Atmosphérique Régional (MAR), a regional climate model. I compare MAR model output with satellite imagery from the Moderate Resolution Imaging Spectroradiometer (MODIS) to isolate differences between modeling and remote sensing data and highlight regions for climate model improvement. Focusing on both the historic and present-day behaviour of the GrIS through a multidisciplinary approach allows me to more broadly investigate the processes governing historic, present-day and future ice mass loss and associated sea level rise.

# Contents

<b>1 Investigating Holocene ice margin retreat and readvance in Southwest Greenland using GIA modeling, Holocene sea level records, geodetic observations and a present-day tide gauge record</b>	<b>3</b>
1.1 Introduction . . . . .	4
1.1.1 Holocene evolution of the GrIS . . . . .	5
1.1.2 Present-day sea level change and ice mass loss in Greenland . . . . .	7
1.2 Background . . . . .	8
1.2.1 Relative sea level and glacial isostatic adjustment . . . . .	8
1.3 Method . . . . .	9
1.3.1 GIA model . . . . .	9
1.3.2 Contributors to present-day RSL rate . . . . .	13
1.3.3 Observational data . . . . .	14
1.4 Results and discussion . . . . .	14
1.4.1 Modeled RSL responses in Nuuk . . . . .	14
1.4.2 Modeled present-day RSL rates in Nuuk . . . . .	17
1.4.3 Tide gauge . . . . .	21
1.4.4 Literature analysis of RSL contributions . . . . .	22
1.4.5 Comparison of RSL rates . . . . .	24
1.5 Conclusion . . . . .	26
<b>2 The role of bare ice extent and albedo variability on runoff from the Greenland Ice Sheet</b>	<b>27</b>
2.1 Introduction . . . . .	28
2.2 Background . . . . .	29
2.2.1 Greenland Ice Sheet mass balance . . . . .	29
2.2.2 Bare ice and albedo feedbacks . . . . .	29
2.3 Method . . . . .	31
2.3.1 ELA estimate . . . . .	32
2.3.2 Bare ice extent . . . . .	32
2.3.3 Albedo . . . . .	32
2.3.4 Runoff . . . . .	33
2.4 Results and discussion . . . . .	34
2.4.1 Inter-annual bare ice extent . . . . .	34
2.4.2 Intra-annual bare ice extent . . . . .	36
2.4.3 Bare ice albedo . . . . .	37
2.4.4 Runoff . . . . .	40
2.5 Conclusion . . . . .	40
<b>Appendices</b>	<b>42</b>
<b>A Sea level equation</b>	<b>42</b>
<b>References</b>	<b>45</b>

# 1 Investigating Holocene ice margin retreat and readvance in Southwest Greenland using GIA modeling, Holocene sea level records, geodetic observations and a present-day tide gauge record

## Abstract

Global coastlines are changing drastically due to sea level rise in response to recent climatic changes. Ice melt from the Greenland Ice Sheet (GrIS) is a major contributor to the present-day and future sea level rise. However, the future contribution from the GrIS remains uncertain. Understanding the response of the GrIS to historic warming can improve projections of its future behaviour. Temperatures around Greenland during the Holocene Thermal Maximum were several degrees higher than today and especially Southwest Greenland has been exposed to a warmer climate during this period. It is suggested that the ice margin retreat in Southwest Greenland has retreated beyond its current position in response to this warming and later readvanced when temperatures dropped. However, the precise magnitude and timing of this retreat remains unknown as recent literature suggests little to no retreat in Southwest Greenland. In this study I investigate the sensitivity of the GrIS to warming during the Holocene Thermal Maximum. In particular, I provide constraints on the late-Holocene ice margin retreat and readvance in Southwest Greenland. I use a glacial isostatic adjustment (GIA) model paired with a range of 1D and 3D viscoelastic Earth structures and two ice sheet models, ICE6G and Huy3. Both ice sheet models incorporate a different estimate of the magnitude and timing of the ice margin retreat and readvance, derived using different methodologies and data sets. However, the correctness of the ice margin retreat modeled in ICE6G and Huy3 remains unclear. Therefore, both ice sheet models are used in their original form and in an altered form in which the late-Holocene ice margin retreat and readvance in Southwest Greenland is omitted. These alterations to the ice sheet models are used to isolate and investigate the effect of ice margin retreat on the modeled relative sea level response in this area. The modeled relative sea level response is compared to paleo sea level observations in the area surrounding Nuuk to explore the trade-offs between Earth structure and ice reconstruction. Next, I extract the predicted present-day solid Earth deformation from my GIA models and compare it to the present-day uplift measured by the Nuuk GNET station (2009-2015) after it has been corrected for elastic effects. Lastly, I compare my model predictions of present-day sea level change to observations from a tide gauge in Nuuk (1958-2002) after it has been corrected for non-GIA contributors to present-day sea level change (contemporary ice melt, steric effects and terrestrial water exchange). Each data set allows me to constrain the GIA model suite (ice and solid Earth parameters). In particular, I investigate what timing and amount of ice margin retreat and readvance is permitted by the data. Results show that some degree of late-Holocene ice margin retreat in Southwest Greenland is necessary. However, this might be smaller than what has been suggested by Huy3.

## 1.1 Introduction

By the end of this century more than 150 million people will have lost their homes as a direct consequence of rising sea level and yet it remains unknown exactly how much and how fast sea level will rise, which ice sheets are most vulnerable to collapse, and how the world's coastlines and islands will respond to this change (Kopp et al., 2017). To understand how sea level will respond to future warming we can investigate how ice sheets have responded in the geologic past when temperatures were naturally warmer than today (Fischer et al., 2018). In this thesis I will focus on the southwestern region of the Greenland Ice Sheet (GrIS), which is an area of major contemporary ice mass loss (Broeke et al., 2009). In the first part of this thesis I use a variety of data sets to better understand how sensitive this area of the GrIS was to warming during the Holocene. In the second part of my thesis I investigate what implications this ice sheet evolution has for our interpretation of present-day ice melt.

During the Holocene Thermal Maximum (HTM;  $\sim 11-5$  ka), temperatures around Greenland were 1-4°C higher than today (Fischer et al., 2018) and it remains unclear how much the GrIS has retreated in response to this warming. Ice sheet models that are forced under warmer-than-present HTM temperatures lead to substantial ice margin retreat during this time period. Figure 1.1 shows the ice margin chronology for ice sheet model Huy3 (Lecavalier et al., 2014) between 16 ka and present, indicating an ice margin retreat of 40-60 km around 4 ka in the Southwest, followed by a readvance to the current position. This retreat and readvance has also been required to match paleo sea level observations in this region (Figure 1.1; Lecavalier et al., 2014). In order to predict sea level change in response to a changing ice sheet one needs to account for glacial isostatic adjustment (GIA), which is the viscoelastic response of the solid Earth, change in gravity field and change in rotation axis to a changing ice and ocean mass load. These results of a significant retreat and readvance are seemingly at odds with recent reconstructions of the ice sheet margin, which suggest little to no retreat with a maximum of 10 km beyond the present ice margin (Young and Briner, 2015). In the first part of this thesis I will investigate the question: *How much ice margin retreat and readvance is consistent with constraints on the evolution of the ice sheet margin while simultaneously fitting paleo sea level records in this region?* To investigate this question I will use a GIA model to understand what processes drive sea level change along the southwestern margin of Greenland by investigating different contributors to GIA and varying model parameters. In particular, I will vary the ice margin retreat and readvance in Southwest Greenland to elucidate the effect of this ice margin chronology on the fit to paleo sea level records. While varying the ice margin chronology, I use a range of 1D and 3D viscoelastic Earth structures to investigate what Earth structures provide a fit to the paleo records for a given ice margin chronology. These results will allow me to decipher the different drivers of past sea level change in this region and put bounds on the sensitivity of the GrIS to mid-Holocene temperatures.

The effects of past changes in the GrIS are still causing contemporary deformation and sea level change around Greenland today, which contaminates geodetic and tide gauge records that are aimed at detecting current mass loss from the ice sheet (Spada et al., 2014 and Khan et al., 2016). In the second part of my thesis I will investigate the question: *What is the contribution of GIA to current sea level change and solid Earth deformation?* To estimate this contribution I use the GIA model that is constrained with Holocene observations. Combining these with tide gauge data from Nuuk allows me to investigate mass loss from the GrIS over the past decades. In this thesis I focus on Nuuk as it is located in the center of the supposed ice margin retreat region and because it is most abundant in observational data.

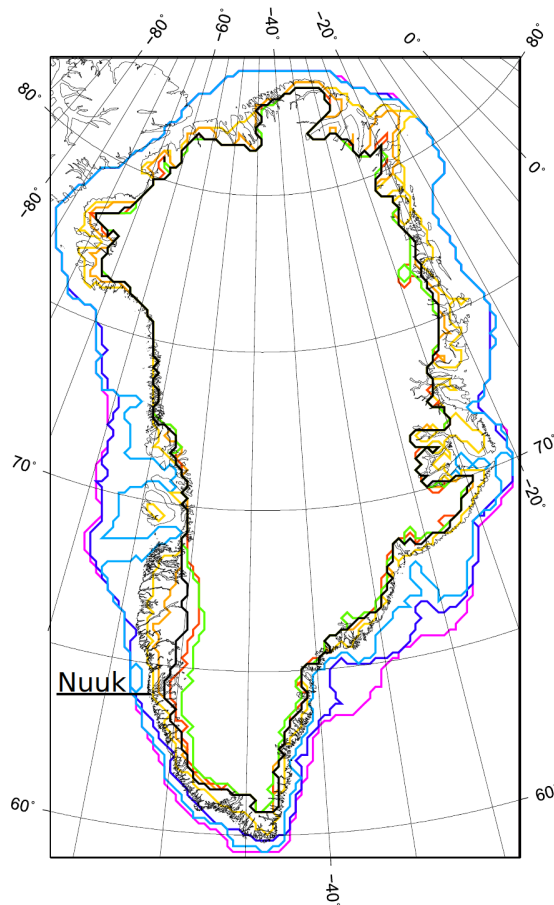


Figure 1.1: Huy3 ice margin chronology of the GrIS. The location of Nuuk is indicated in the Southwestern region. Pink: 16ka, dark blue: 14ka, light blue: 12ka, yellow: 10ka, orange: 9ka, red: 6ka, green: 4ka, black: present. *From Lecavalier et al., 2014.*

### 1.1.1 Holocene evolution of the GrIS

The Last Glacial Maximum (LGM; 26.5-20 ka) denotes the most recent peak of global ice volume and an accompanying global mean sea level low stand of  $\sim 120$  m below the present-day level (Clark et al., 2009 and Austermann et al., 2013). Since the LGM, global temperatures have risen in response to increased northern hemispheric Summer solar radiation, commencing global ice melt (Clark et al., 2009). During the HTM, temperatures in Greenland rose rapidly (Dahl-Jensen et al., 1998), inducing significant melt and retreat of the Greenland ice margin. The southwestern region of the GrIS responded most severely to the HTM warming, resulting in an inland retreat beyond its current position during the middle to late Holocene (Tarasov and Peltier, 2002, Kaufman et al., 2004 and Simpson et al., 2009). Multiple studies using observational data and/or modeling have investigated this ice margin chronology and suggested a retreat and readvance of 10-100 km behind its current margin some time between 8 and 1.8ka. Table 1.1 provides an overview of the current literature on the Holocene retreat and readvance and demonstrates that estimates vary widely. Understanding the behaviour of retreat is essential as it helps us to understand the sensitivity of the ice sheet to warming.

Constraints on the ice behaviour come from past and present ice margin extents, ice cores, radiocarbon dating, sedimentation, and other geophysical and geological observations (e.g. Weidick et al., 1990, Willemsse et al., 2003, Forman et al., 2007, Briner et al., 2010 and Storms et al., 2012). These observation-based studies provide constraints on the timing of the ice margin retreat behind its current position and on the timing of

the readvance to its current position. Because the current extent of the ice sheet impedes collection of field data inland of the present-day ice margin, direct observational data of the retreat and readvance pattern is not available.

A different approach to constraining the retreat and readvance is modeling the effect of ice loading and unloading on the solid Earth and comparing it to relative sea level (RSL) observations (e.g. Tarasov and Peltier, 2002, Tarasov and Peltier, 2003, Fleming and Lambeck, 2004, Simpson et al., 2009, Lecavalier et al., 2014 and Young and Briner, 2015). RSL reconstructions in the southwestern region of Greenland follow a characteristic J-shape, indicating a multi-millennial dip below the current RSL. It is suggested that this J-shape is a combined product of processes related to RSL change and GIA associated with, mainly, the ice mass changes of the GrIS and the Laurentide Ice Sheet (LIS). This J-shape is indicative of an ice margin retreat in Southwest Greenland beyond its current extent (Fleming and Lambeck, 2004, Simpson et al., 2009 and Lecavalier et al., 2014). Lecavalier et al., 2014 used this modeling approach in which they used a climate-forced ice sheet model to reconstruct the ice margin chronology and this resulted in the ice sheet model Huy3. Such ice sheet reconstructions are, however, non-unique and, in the case of Lecavalier et al., 2014, model fit to RSL observations requires (regional) modifications to climate and sea-level forcing. Furthermore, they suggest a significant improvement in RSL data-model fit can be achieved by adopting laterally heterogeneous solid Earth parameters around Greenland. Additional factors of uncertainty originate from: 1) missing physics and sub-grid processes such as calving, grounding line migration, ice streams and outlet glacier dynamics; 2) insufficient ice sheet model resolution; and 3) non-Greenland ice, specifically the representation of the LIS, whose solid Earth deformation effects are prominent along the western margin of Greenland due to its close proximity to the LIS (Lecavalier et al., 2014). In other words, the solution to fitting the modeled RSL signal to the currently available set of observational constraints is non-unique.

<b>Study</b>	<b>Timing</b>	<b>Retreat</b>
Weidick et al., 1990	Start and end at 4.7 - 2.7 ka	> 15 km
Tarasov and Peltier, 2002 Tarasov and Peltier, 2003	Minimum at 8 ka	~ 100 km
Willemse et al., 2003	Start and end at 3.4 - 0.55 ka	> 15 km
Fleming and Lambeck, 2004	Minimum at several ka	40 km
Forman et al., 2007	End at 2 ka	
Simpson et al., 2009	Minimum at 5 - 4 ka	80 km
Briner et al., 2010	Start and end at 7.3 - 2.3 ka; Minimum at 6 - 5 ka	10s of km
Storms et al., 2012	Minimum at 4 ka	
Lecavalier et al., 2014	Minimum at 4 (5 - 3.5) ka; Start of retreat at 8 - 6 ka	40 - 60 km
Young and Briner, 2015	4.2 - 1.8 ka	10 km

Table 1.1: Overview of current literature on the extent and timing of the Holocene ice margin retreat in Southwest Greenland.

One goal of this thesis is to determine how much retreat and readvance in Southwest Greenland occurred during the middle to late Holocene. As direct observational data inland of the present-day ice margin is not available, I will use Holocene sea level records in the surrounding area and two ice sheet models, ICE-6G\_C (Argus et al., 2014 and Peltier et al., 2015) and Huy3 (Lecavalier et al., 2014), as a means to estimate the extent of the ice margin chronology during periods for which no observational data is available. The ice

sheet models are used as input for the GIA model with which RSL is computed. Next, I adjust ice margin chronologies to investigate the effect of the retreat and readvance on the RSL signal and their fit to sea level observations. Similar approaches for reconstructing the glacial and deglacial patterns of ice sheets have been well established (e.g. Peltier and Andrews, 1976, Lambeck et al., 1990 and Fleming and Lambeck, 2004). Earth structure and rheology parameters strongly affect the magnitude and timing of GIA induced by ice loading and unloading (e.g. Lecavalier et al., 2014, Spada et al., 2014, Wake et al., 2016 and Milne et al., 2018). These Earth structure and rheology parameters are not yet fully constrained globally, nor in the vicinity of Greenland (Fleming and Lambeck, 2004). Here, I explore both 1D and 3D solid Earth and rheology parameters to investigate what role these parameters play in the RSL signal.

### 1.1.2 Present-day sea level change and ice mass loss in Greenland

While GIA significantly contributed to local sea level change during the Holocene, the adjustment to ice changes during this period is still ongoing today. This contamination from GIA introduces uncertainties in estimating ice melt from tide gauges and satellite records (Khan et al., 2016 and Sutterley et al., 2014). Global mean sea level (GMSL) rise has accelerated from 1.5 [1.3 - 1.7] mm yr<sup>-1</sup> during 1901-1990 to 3.2 [2.8 - 3.6] mm yr<sup>-1</sup> during 1993-2010. Greenland is one of the major contributors to this rise with an increasing rate from 0.09 [-0.02 - 0.20] mm yr<sup>-1</sup> during 1992-2001 to 0.59 [0.43 - 0.76] mm yr<sup>-1</sup> during 2002-2011 (Church et al., 2013). Besides the long-term viscoelastic response to ice mass changes since the LGM, sea level responds to present-day ice mass changes through an elastic response of the solid Earth. Furthermore, changes in gravitational attraction to ice mass and solid Earth induce instantaneous changes in sea level. Observations from tide gauges have long been recognized as powerful tools for studying GMSL as well as regional sea level changes (Gutenberg, 1941), especially for the pre-satellite era (Spada and Galassi, 2012 and Spada et al., 2014). Correction of a tide gauge record from Nuuk (1958-2002) for long-term adjustments associated with ice mass changes since LGM allows for evaluation of ice mass changes during the observation period. This is an approach previously used by Spada et al., 2014. In this study they produced estimates of the various contributors to local sea level change around Nuuk from GIA modeling, literature and sea level fingerprinting. The sum of these contributions is compared to the sea level rate derived from the Nuuk tide gauge. The authors found that their modeled sea level rate is lower than the tide gauge-derived sea level rate and suggested this is due to an improper estimate of the contemporary ice mass change. They suggested that the mass balance of the GrIS during 1958-2002 may therefore have been closer to balance than suggested by previous studies. However, a significant uncertainty remains in their estimated GIA contribution, i.e. their estimate of sea level response since the LGM. This possibly contributed to the data-model misfit. For a more robust conclusion regarding the mass balance of the GrIS during 1958-2002, an improved estimate of the GIA contribution is necessary.

In the second part of this thesis I investigate the mass loss of the GrIS over the last decades by reassessing the conclusions drawn by Spada et al., 2014. I re-evaluate the contributions of the tide gauge record in Nuuk, focusing on the long-term contribution since the LGM by using the GIA model and modifications as in the previous section. Additionally, I will update the remaining constituents of the RSL signal with current literature estimates.

## 1.2 Background

### 1.2.1 Relative sea level and glacial isostatic adjustment

Sea level change can refer to either global or relative sea level change. Here, global mean sea level change is the change in global ocean volume due to, for instance, addition of melt water or steric effects. Relative sea level is measured locally as the distance between the ocean floor and the ocean surface. This is the sea level that is measured by tide gauges as they are mounted on the Earth's surface, thus including vertical displacement of the Earth in their measurements.

Relative sea level change is driven by many processes, as shown in Figure 1.2a. Sea level change through steric effects is currently the largest contributor to global mean sea level rise (Church et al., 2013). These effects include changes in density of the ocean water through temperature and salinity variations, which affect the total volume occupied by the water. In a warming climate, ocean water acts as a heat sink. An increase in heat in ocean water results in a decrease in density and subsequent increase in volume. Moreover, a decrease in salinity, due to an influx of fresh water from ice sheet melt for instance, also leads to a decrease in density. Both processes thus add to a rising sea level.

Land ice sheets and glaciers can store large amounts of water mass and the total ocean water mass is thus partly controlled by water exchange between ocean and ice sheets and glaciers. Additional sources of water on continents are snow, permafrost, groundwater and lakes. Changes in these water sources are collectively termed terrestrial water mass exchange. These water mass exchanges have a non-uniform influence on sea level through gravitational, rotational and solid Earth deformation effects. The viscoelastic response of the solid Earth, together with the gravitational and rotational changes due to a changes in ice and ocean mass load are collectively called glacial isostatic adjustment (GIA).

For gravitational effects, this especially holds for changes in ice sheet mass. Due to their sheer size and mass, ice sheets attract ocean water mass through gravitational effects. This effect will result in an uplift of ocean water height in the vicinity of an ice sheet. therefore, a decrease in the mass of the GrIS will globally lead a sea level rise due to addition of melt water, though in the vicinity of the ice sheet it may result in a sea level drop as the gravitational attraction of the ice sheet diminishes (Hay et al., 2014).

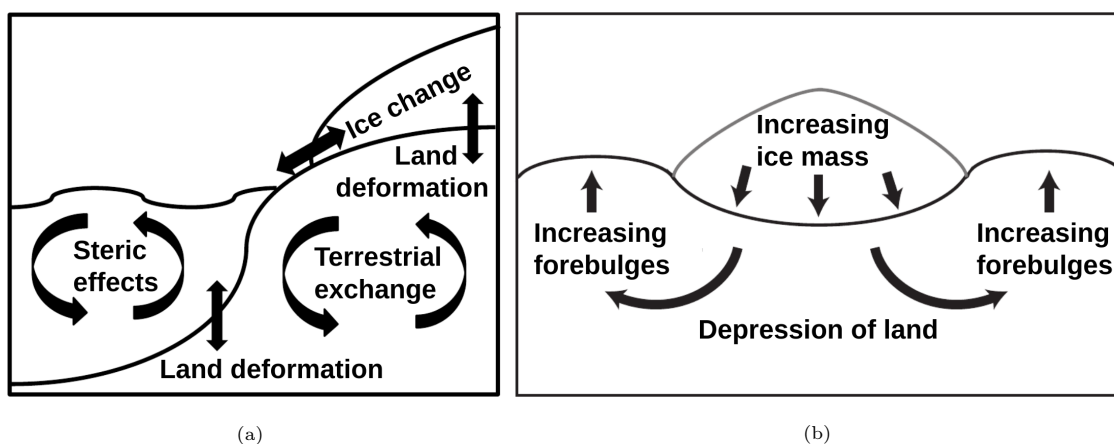


Figure 1.2: Schematic figures of: a) processes driving relative sea level; and b) depression of the solid Earth underneath an ice sheet and the subsequent rise of forebulges. Adapted from Slangen, 2012.

A redistribution of ice and ocean mass will also affect the magnitude and orientation of the Earth's rotation axis (Milne and Mitrovia, 1998). Earth's rotation vector will move towards a region of mass loss from, for instance, a decreasing ice sheet. A change in the orientation of the rotation vector will alter the shape of the geoid and the solid Earth through centrifugal forces, thereby affecting sea level (Whitehouse, 2018).

Furthermore, a change in mass loading at the Earth's surface will induce solid Earth deformation. A changing ice sheet volume and mass will lead to a changing pressure on the underlying crust and mantle, resulting in solid Earth deformation in the form of vertical land motion. The deformation of the solid Earth is a viscoelastic process, combining elastic (instantaneous) and viscous (delayed) behaviour. The initial response of the mantle to a change in mass loading is elastic, leading to an almost instantaneous uplift or depression. A delayed response to this same change in mass loading is the viscous response, which acts on time scales of thousand of years (Vermeersen and Schotman, 2009). During a glacial period, large ice sheets are formed, increasing mass loading and depressing the mantle locally, as shown in Figure 1.2b. Lithospheric material is not only depressed, but also flows laterally and upwards in the periphery of the ice sheet, forming forebulges (or peripheral bulges) and locally uplifting the solid Earth. Conversely, a melting ice sheet induces the reversed process; uplifting the solid Earth underneath the ice sheet and decreasing bulges.

### 1.3 Method

To evaluate Holocene ice margin retreat and readvance in Southwest Greenland I will determine the RSL response in this region to a changing global ice mass load since the Eemian (130-115 ka) using a GIA model. I will utilize a range of possible scenarios regarding the ice margin chronology in Southwest Greenland and Earth's viscoelastic structure. First, I will focus on the RSL response during the Holocene and compare the GIA model output to paleo sea level observations. Then, I will focus on the contemporary RSL rate and compare the modeling results to RSL rates derived from contemporary tide gauge data. These comparisons will allow me to provide constraints on the ice margin chronology in Southwest Greenland and Earth's viscoelastic structure. I will focus on the region surrounding Nuuk, as this region is located in the center of the supposed region of ice margin retreat and multiple sets of observational data are available in this area.

Furthermore, the findings regarding ice margin chronology and Earth's viscoelastic structure will allow me to evaluate the contemporary contribution of GIA to current sea level change and solid Earth deformation. Combining these results with literature estimates of the other contributors to sea level change and the most recent tide gauge data from Nuuk, I will be able to assess mass loss from the GrIS over the past decades.

#### 1.3.1 GIA model

##### Earth model

The GIA model used in this thesis determines the RSL response as a result of changing ice mass loading by globally solving the the sea level equation (SLE) described in Appendix A. Several Earth models with a range of laterally homogeneous viscoelastic Earth structures are utilized to calculate the RSL response. All Earth models have the upper-lower mantle boundary at 670 km. The GIA model is based on a pseudo-spectral approach and run with a maximum spherical harmonic degree and order of 256. The density and elastic properties of the solid Earth are provided by the 1D Preliminary Reference Earth Model from the surface to the center of the Earth (Dziewonski and Anderson, 1981). The viscoelastic structure of the Earth model is described by a lithosphere (LT) with an elastic thickness of either 71 or 96 km, an upper mantle viscosity (UMV) ranging from  $0.2-0.5 \cdot 10^{21}$  Pa·s, and a lower mantle viscosity (LMV) ranging from  $5-40 \cdot 10^{21}$  Pa·s. For brevity, the combinations of viscoelastic structures are abbreviated. For example, 71-0.5-10 represents an LT of 71 km, a UMV of  $0.5 \cdot 10^{21}$  Pa·s, and an LMV of  $10 \cdot 10^{21}$  Pa·s. These ranges of Earth parameters

provide a means of isolating and evaluating the effect of each parameter on the RSL response. Furthermore, specific values of the 1D, i.e. depth-dependent only, viscoelastic structure from previous studies are added to the analysis: 1) 120-0.5-2 (Lecavalier et al., 2014), 2) 90-0.5-2.7 (Peltier, 2004), and 3) 80-0.4-10 (Fleming and Lambeck, 2004). This provides the opportunity to evaluate the effect of a change in ice margin chronology on viscoelastic Earth structures assessed as good estimates by previous studies.

Additionally, three radially and laterally heterogeneous viscoelastic Earth structures are adopted in the analysis. These viscoelastic structures consist of global 3D variations of the lithospheric thickness and upper and lower mantle viscosities to the following average values: 1) 80-0.5-5, 2) 100-0.5-5, 3) VM5 (Peltier and Drummond, 2008). The viscosity variations are derived from seismic tomography by Richards et al., 2020. As the velocity of seismic waves is sensitive to temperature and rheology, seismic tomography is a direct tool for imaging shear wave velocity in the mantle. The shear wave models from Schaeffer and Lebedev, 2013 and Schaeffer and Lebedev, 2014 are used for the upper 400 km of the mantle and the shear wave model from French and Romanowicz, 2014 is used for below 400 km depth to provide features in the temperature and viscosity perturbations. In the upper 400 km of the mantle, the scaling is based equations that transform shear wave velocity to viscosity from Yamauchi and Takei, 2016. These equations are derived from laboratory experiments in which the authors pressurized material and measured the associated change in shear wave velocity, temperature and viscosity. Although the authors provide relationships between shear wave velocity and temperature and viscosity, the actual constants and parameters in the equations are not well constrained. This is in part a result of their use of material analogous to rock for their experiments instead of the actual mantle material. It is therefore necessary to find fitting parameters to use these equations. These parameters are determined by calibrating the equations with values of and constraints on the thermal structure of oceanic lithosphere, the average adiabatic gradient within the convecting mantle, the attenuation structure of the upper mantle beneath old oceanic lithosphere, and the bulk diffusion creep viscosity of the upper mantle from previous GIA studies. Incorporating these values and constraints allows for calibrating a set of parameters within the shear wave velocity to temperature to viscosity equations. With the equations and associated constants and parameters, the viscosity variations can be calculated from shear wave velocity. Below 400 km, a different approach is used because sensitivity of surface waves to velocity structure drops and the number of independent constraints on mantle properties is more limited. In this case, the mantle composition is assumed to be pyrolytic allowing for calculation of temperature using the mineral physics toolbox Perplex (Connolly, 2005). Then, an Arrhenius equation and associated parameters from Steinberger and Calderwood, 2006 are used to calculate viscosity variations from temperature variations.

The 3D model runs in this study do not contain nor propagate uncertainties. Due to the limited scope of this study, I use three sets of 1D reference values for the lithospheric thickness and upper and lower mantle viscosity. The 3D lithospheric thickness and viscosity variations are projected onto these reference values. In a more extensive study I would include uncertainties in the constraints and assumptions made in calculating the viscosity variations to produce a range of 3D models. This range of 3D models is then used to calculate a range of GIA predictions, which in turn is used to determine RSL response. More careful consideration of the constraints and assumptions used in calculating the viscosity variations would be necessary for this method. It is worth noting that these runs are significantly more expensive computationally and require learning the use of an entirely different model code which did not fit in the scope of this study.

Figure 1.3 depicts the lateral heterogeneity of the lithospheric thickness as used for the LTO and F3D model runs. It shows a relatively thick lithosphere around Nuuk compared to the reference value of 100 km. Figures 1.4a and 1.4b depict the lateral viscosity variations at 200 and 900 km depth, representing the upper and lower mantles, respectively. No significant deviations from the average viscosity value are apparent at 200

km depth around Nuuk, while lower viscosity values are present in the lower mantle in this area. Lateral viscosity variations are at least in the order of  $10^4$  Pa·s around Greenland, shown by the range in viscosity variation values at 200 km depth. This range is significantly larger than the range of viscosity values used in the 1D Earth model runs, which is in the order of  $10^2$  Pa·s, supporting the use of these 3D model runs.

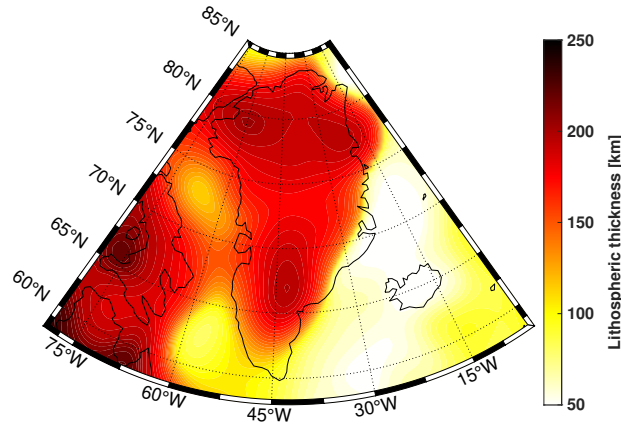


Figure 1.3: Lateral variations of the lithospheric thickness around Greenland.

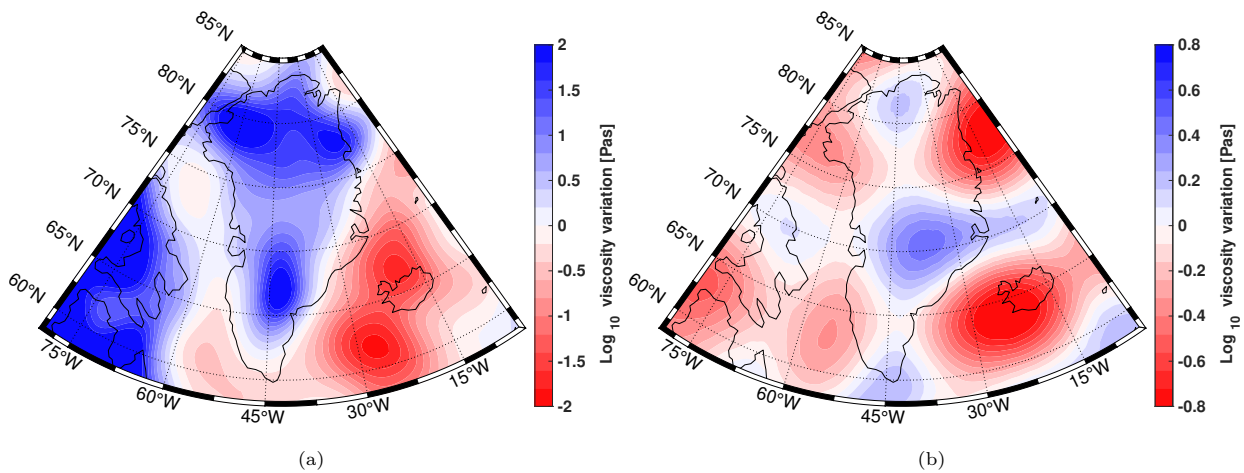


Figure 1.4: Lateral viscosity variations around Greenland at depths: a) 200 km, and b) 900 km.

### Ice sheet models

I will use two ice sheet models as input for the GIA model, ICE-6G\_C (hereafter called ICE6G) and Huy3. Both ice sheet models provide ice thickness values between 122 ka and present, with time steps ranging from 2-6 ka before the Holocene and 0.25-0.5 ka during the Holocene. ICE6G and Huy3 are different in the global glaciation and deglaciation patterns of grounded continental ice sheets they describe as well as their methodologies for deriving these patterns.

ICE6G is not a physical ice sheet model in the sense that it does not incorporate any ice sheet physics in the model. Rather, ice masses in ICE6G are manually readjusted to fit certain data sets (Argus et al., 2014, Stuhne and Peltier, 2015 and Peltier et al., 2015). A few RSL signals and geodetic measurements of the present-day vertical and horizontal crustal motion are used to determine what history of ice thickness variations should be associated with the observations by solving the SLE. These solutions of the ice thickness

reconstructions in ICE6G are, however, non-unique. ICE6G determines ice thickness histories of all global ice, except for the history of the GrIS, which is taken from the Gr.B model described by Tarasov and Peltier, 2002 and Tarasov and Peltier, 2003.

Huy3 (Lecavalier et al., 2014) is constructed based on an initial 3D thermo-mechanical ice sheet model (Huybrechts and Wolde, 1999 and Huybrechts, 2002). This glaciological model is used to simulate the evolution of the GrIS from the Eemian until present and is forced with climate (GRIP  $\delta^{18}\text{O}$ ) and ocean variations. Lecavalier et al., 2014 use a GIA model and input their ice reconstruction together with a viscoelastic Earth structure to predict vertical land motion and RSL responses by solving the SLE around Greenland. They constrain the ice model to fit the predicted RSL responses to RSL observations along the margins of the GrIS. This ice model for the GrIS is then combined with an ice model for the North American ice sheet (Tarasov et al., 2012) and the remaining global ice is taken from ICE5G (Peltier, 2004), a predecessor of ICE6G.

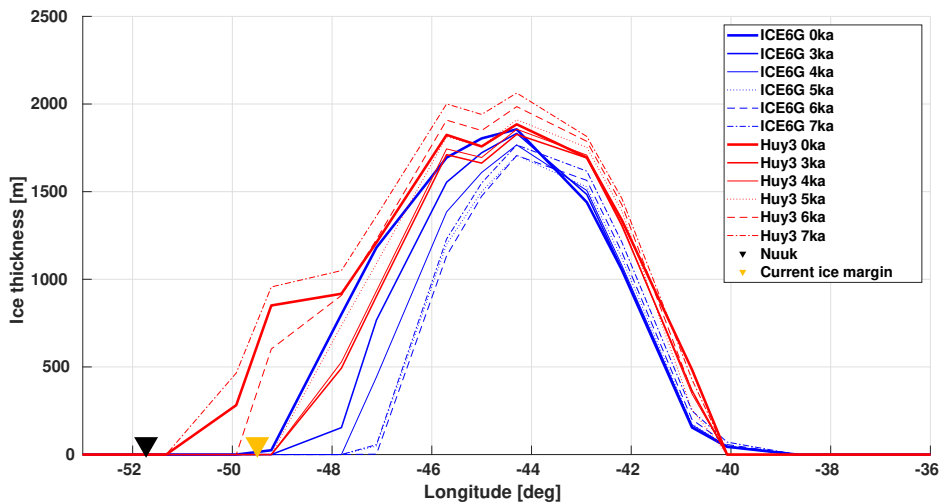


Figure 1.5: Zonal cross sections of the margin chronologies over Nuuk at latitude of 64.17N from 7 ka to present for both ICE6G (blue) and Huy3 (red).

Of specific interest is the difference in ice margin chronology in Southwest Greenland between ICE6G and Huy3. Figure 1.5 shows cross sections of the ice sheet at a latitude of 64.17N from 7 ka to present for both ICE6G and Huy3. This shows that between 7 ka and present, Huy3 describes an ice margin near Nuuk about 2 degrees ( $\sim 100$  km) further west than ICE6G does. Furthermore, the figure shows that ICE6G provides a better fit to the present-day ice margin, shown by the position of the orange marker. Lecavalier et al., 2014 illustrate in their Figure 13 the bias in present-day ice thickness of the GrIS, as observed and as modeled by their Huy3 ice sheet model. The authors argue that their model fits the observed present-day ice thickness well in the interior, but acknowledge that a significant overestimation of Huy3 along the margins of the GrIS exists. They argue that this overestimate in ice volume stems from an incorrect evolution of the ice margin. Ice sheet margins may exhibit steep horizontal gradients and therefore small differences in ice margin position may thus lead to large differences in ice thickness. Moreover, this discrepancy may result in an incorrect RSL prediction because Huy3 captures the present-day loading incorrectly. Furthermore, ICE6G describes a minimum ice margin (i.e. maximum retreat) in this region around 6 ka, while this minimum occurs around 3-4 ka for Huy3. To evaluate the effect of ice margin chronology on the RSL response, I augment the original versions of the ice sheet models with an adapted ice sheet history. The original models include their respective ice margin chronologies (Figure 1.5). The adapted models describe

an altered GrIS ice thickness that is constant from 8 ka to present to emulate the exclusion of an ice margin retreat in Southwest Greenland, mimicking the present-day ice margin of the respective ice sheet model.

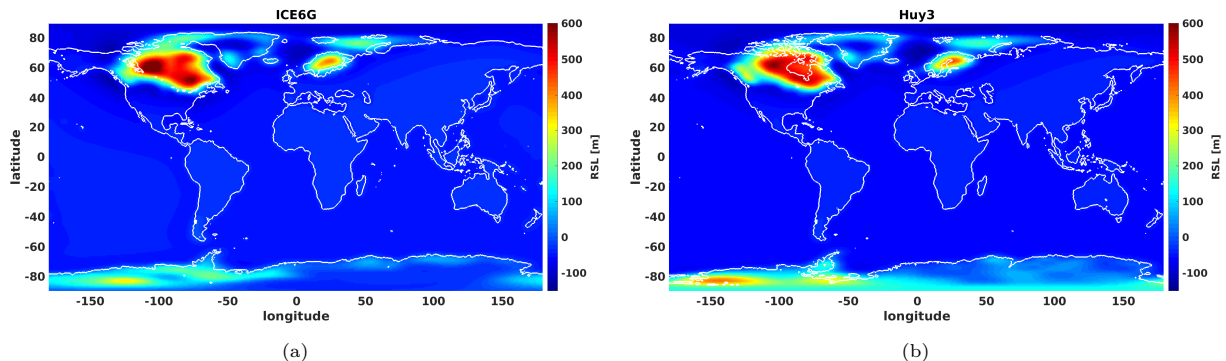


Figure 1.6: Modeled global RSL maps at 12 ka using ICE6G (left) and Huy3 (right) with a viscoelastic Earth structure of 120-0.5-2.

While Figure 1.5 illustrates the discrepancies in local ice margin chronology in Southwest Greenland, additional differences exist globally. This results in different patterns of RSL responses, as shown by the global RSL maps at 12 ka in Figure 1.6, computed using both ICE6G and Huy3 paired with a viscoelastic structure of 120-0.5-2. For instance, ICE6G has a larger LIS than Huy3 during the LGM, which leads to a larger and higher magnitude negative RSL response over North America than. Conversely, Huy3 describes a larger West Antarctic Ice Sheet than ICE6G during the LGM, leading to a larger and higher magnitude negative RSL response in this region. These differences in ice sheet thickness in the far-field can have a significant effect on the local RSL in Greenland through eustatic sea level change and the viscoelastic response of peripheral bulges.

### 1.3.2 Contributors to present-day RSL rate

The RSL rate ( $r$ ) obtained from a tide gauge record represents the total RSL rate as described by Spada et al., 2014 in their Equation 2, which is repeated here:

$$r^{OBS} = r^{GIA} + r^{GrIS} + r^{AIS} + r^{GIC} + r^{TER} + r^{STE} + r^{TEC}. \quad (1.1)$$

The total RSL rate includes effects due to GIA and due to present-day changes in GrIS, Antarctic Ice Sheet (AIS), glaciers and ice caps (GIC), terrestrial mass exchange (TER), steric effects (STE) and tectonic deformation (TEC). The GIA component is defined as the ongoing response to ice and ocean mass changes that occurred prior to 1 ka, including eustatic, viscoelastic, gravitational, rotational and steric effects. Tectonic deformation is assumed negligible on time scales of  $10^5$  years (Khan et al., 2016), which is the time considered in this study.

I will use a GIA rate that is obtained from my GIA modeling and I will quantify the remaining contributions of GrIS, AIS, GIC, TER and STE, using the most current literature estimates, to obtain a modeling- and literature-derived estimate of the total RSL rate. All literature-based contributions to the RSL rate are calculated over the period 1958-2002 to match the tide gauge observation period. This will allow me to compare my modeled GIA rate with the tide gauge-derived RSL rate. Additionally, decomposition of the GIA contribution will allow me to evaluate the RSL response resulting from only the solid Earth deformation. This will provide me with an estimate of the pure viscoelastic response and the opportunity to evaluate my

modeling assumptions with the viscoelastic solid Earth deformation obtained by Khan et al., 2016 from geodetic data from a GPS station in Nuuk.

### 1.3.3 Observational data

Four index and two upper-limiting paleo RSL observations, derived from radiocarbon-dated pollen and macrofossil diagrams from lakes at Godthåbsfjord (64.48N, -50.99E; Fredskild, 1983), are used to evaluate the modeled RSL curves at this location near Nuuk. Index points have a well defined relationship of age and elevation to former sea level, while upper-limiting data merely provide limiting constraints. The paleo RSL observations contain 2-sigma error bounds in both age and elevation.

To evaluate the RSL rates as modeled using both ICE6G and Huy3 I use independent tide gauge data at Nuuk (64.17N, -51.73E), extracted from the PSMSL database on 20 July 2020. I use two tide gauge records for the periods 16 May 1958 to 16 April 2002 (monthly mean data) and 5 July 2014 to 30 June 2020 (hourly data). Both tide gauges are located at the same position  $\sim 50$  km southwest of the paleo RSL observations. The RSL rate is extracted from the tide gauge records by removing the tidal signals. The Tide Model Driver (TMD; Erofeeva et al., 2020) on 5 km horizontal resolution is used to produce tidal signals at the tide gauge location. The tide model incorporates 24 major and minor constituents representing semidiurnal, diurnal and longer-period tidal signals, as well as the 18.6 y nodal tide. The RSL rate is determined through a linear fit of the data-model difference.

## 1.4 Results and discussion

### 1.4.1 Modeled RSL responses in Nuuk

The RSL response induced by GIA through ice mass loading changes since the Eemian are calculated using both ICE6G and Huy3. Figure 1.7 shows the RSL response between 12 ka and present at the RSL observation site near Nuuk (64.48N, -50.99E), both with and without ice margin retreat and readvance in Southwest Greenland and a range of viscoelastic Earth structures. All RSL responses are shown with respect to present-day sea level. The paleo RSL observations are depicted in the plots, with 2-sigma error bars in timing and height. The crosses are index RSL observations, while the downward triangles are upper-limiting observations. It is clear that the RSL responses differ markedly depending on the modeling assumptions used.

Both ICE6G and Huy3 show an early-Holocene peak which is due to the large global ice volumes leading to low ocean volumes during this time. From the start of the HTM around 11 ka, temperatures rise and global ice volumes decrease, leading to a drop in RSL. This drop continues into a negative RSL dip after which it recovers to the present-day RSL, i.e. the characteristic J-shape. In line with the explanation that the J-shape is caused by the retreat and readvance ice the ice margin in Southwest Greenland, the right column in Figure 1.7 shows that the J-shape disappears when the retreat and readvance is omitted. Placing this in the context of Nuuk's location near the ice margin indicates that the RSL dip is the effect of a reduced gravitational attraction of ocean water towards the ice sheet, as well as the effect of a near-instantaneous local elastic uplifting response to a reducing ice mass load. Furthermore, as Nuuk is located on the peripheral bulge of the LIS, which is currently subsiding in response to ice mass changes since the LGM, a positive contribution to the present-day RSL curve at Nuuk is expected from to this process.

Despite the general similarities, significant differences are observed when changing the ice sheet model from ICE6G to Huy3. Where ICE6G provides an early Holocene peak at  $\sim 10$  ka ranging from 90 to 150 m, Huy3 shows values ranging from 40 to 100 m around this time without a clear peak. A late Holocene dip down to

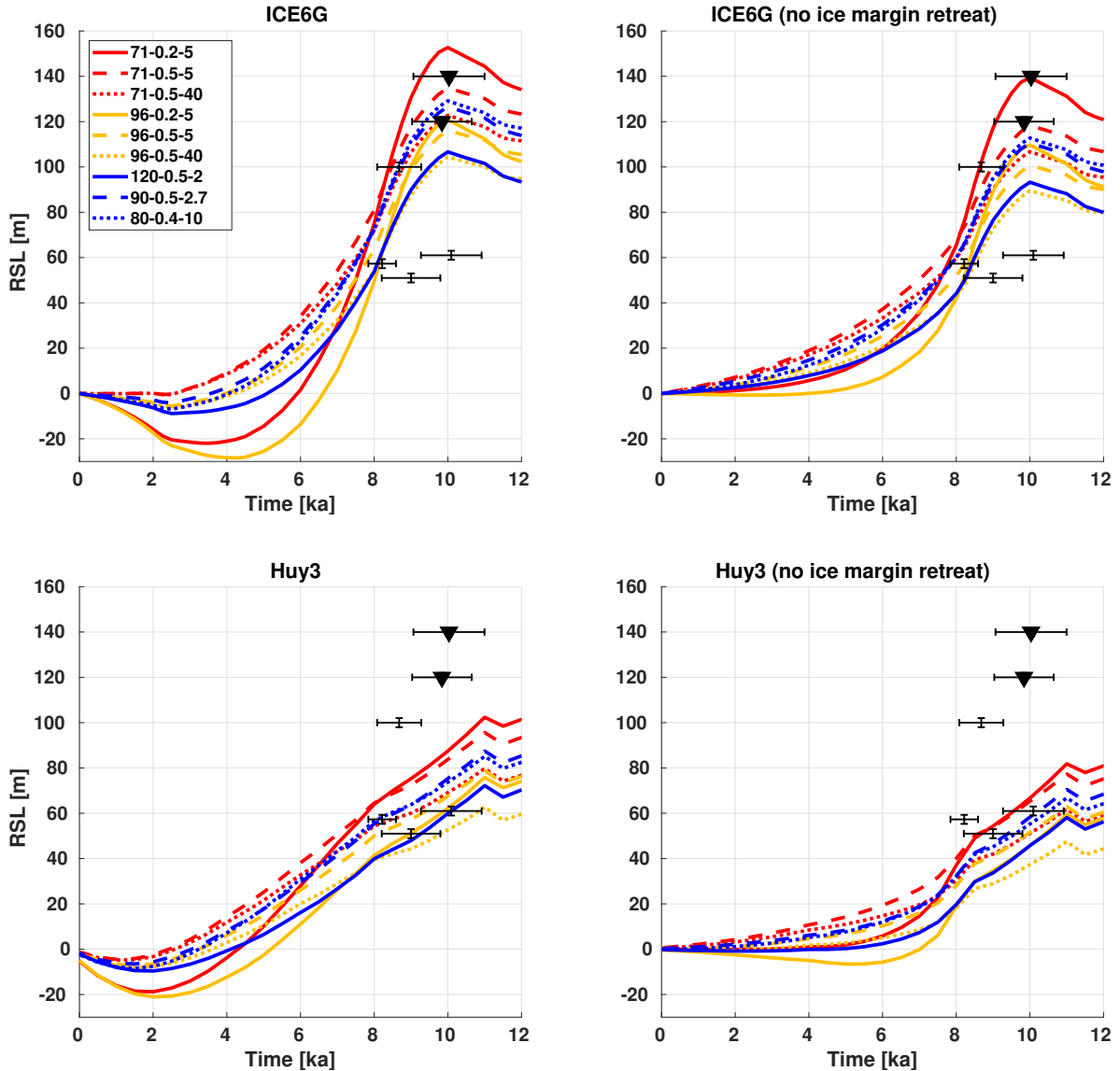


Figure 1.7: Modeled RSL responses due to GIA at Nuuk (64.48N, -50.99E), using ICE6G (top) and Huy3 (bottom). The runs utilize the original amount (left) and no (right) ice margin retreat and readvance. Different colored curves indicate different viscoelastic Earth structures. The paleo RSL observations are index points (cross) and upper-limiting data (downward triangle).

-30 m is found at 2.5-4.5 ka when using ICE6G, while a more recent dip down to -20 m at  $\sim 2$  ka is found for Huy3. These differences are the result of the different ice margin chronologies described by both ice sheet models. The representation of the Southwest Greenland ice margin retreat and readvance plays a key role in the local RSL response through the ice sheet's gravitational attraction and the viscoelastic response of the subsurface. As shown in Figure 1.5, Huy3 models the ice margin in Southwest Greenland  $\sim 100$  km closer to Nuuk between 7 ka and present than ICE6G does. The maximum ice margin retreat in Huy3 occurs around 3-4 ka, while for ICE6G this occurs around 6 ka. A difference in ice margin position of this extent may therefore result in a significantly different RSL response. Moreover, ICE6G and Huy3 incorporate a different representation of the LIS. As Nuuk is located on the peripheral bulge of the LIS, this difference in historic ice thickness of the LIS leads to a minor difference of the contemporary subsidence rate of its peripheral bulge.

The effect of omitting ice margin retreat in Southwest Greenland is illustrated through the difference be-

tween the left and right plots in Figure 1.7, for both ICE6G and Huy3. The effect on the RSL response by omitting ice margin retreat is similar for ICE6G and Huy3. Most prominently is the lack of a RSL dip in the late Holocene when omitting any ice margin retreat, which holds for most viscoelastic structures. Besides affecting the RSL dip, omitting ice margin retreat also reduces the RSL peak in the early Holocene by 10-20 m. This effect is less notable because no changes in the ice margin chronology before 8 ka are made and no direct differences in ice mass loading are therefore induced in this period. These differences in the magnitude of the early-Holocene peak are necessary to maintain a continuous RSL signal over the full period.

Using a variety of viscoelastic Earth structures results in significantly different RSL responses. Again, the effect on the RSL response by varying the viscoelastic Earth structure are similar for ICE6G and Huy3. All four plots in Figure 1.7 show that a low upper mantle viscosity (e.g. 71-0.2-5 and 96-0.2-5) results in a high-magnitude RSL response, with a high early-Holocene peak and a low late-Holocene dip. A less viscous upper mantle is more easily deformed and thus reacts faster and with higher amplitude to changes in local mass loading (Hartmann et al., 2020), indicating that the viscoelastic response induced by a changing GrIS has a higher magnitude for a less viscous upper mantle. A similar trend towards a high-amplitude response is observed for the thin lithosphere (71 km) model runs. This is in line with results from Alaska based on geodetic measurements (DeGrandpre and Freymueller, 2019b), that suggest that more prominent peripheral bulges are attributable to a thin lithosphere as well as a low upper mantle viscosity. Nuuk’s location on the peripheral bulge of the LIS is thus expected to experience an enhanced RSL response for a thin lithosphere and a low upper mantle viscosity. Furthermore, a thin lithosphere may locally result in a higher-amplitude viscoelastic response due to a changing GrIS ice mass loading. However, it is most likely a combined effect of the LIS peripheral bulge and a local deformation underneath the GrIS. Comparing 71-0.5-40 to 71-0.5-5 and 96-0.5-40 to 96-0.5-5 illustrates that a higher lower mantle viscosity merely results in a lower peak at the start of the HTM for all four model variations illustrated in Figure 1.7, while the RSL response in the second half of the Holocene seems to be less sensitive to the lower mantle viscosity. A high-viscosity lower mantle can act as an impenetrable layer which focuses deformation in the upper mantle. The upper mantle may therefore experience more lateral spreading instead of local deformation and peripheral bulge uplift. This leads to a reduction of the vertical amplitude of the deformation rate of both the upper mantle underneath the GrIS, as well as the LIS peripheral bulge.

Figure 1.8 illustrates the effect of laterally heterogeneous viscoelastic Earth structures on the RSL response, modeled with ICE6G. The left plot shows laterally homogeneous viscoelastic structures as a reference, indicated by the prefix '1D'. The plot on the right shows the RSL responses using global 3D variations on top of the reference models, indicated by the prefix '3D', as well as one run with only lateral variations of the lithospheric thickness, indicated by the prefix 'Lith'. Allowing for a laterally varying lithospheric thickness results in a reduced RSL response over the entire Holocene. As discussed earlier, peripheral bulges are less prominent for a higher lithospheric thickness, possibly explaining the lower magnitude of the RSL response for when allowing for lithospheric thickness variations in the early Holocene as Nuuk lies on the peripheral bulge of the LIS. Furthermore, incorporating 3D variations to the background viscoelastic Earth structure results in significantly lower-magnitude RSL responses compared to the 1D reference values (Figure 1.8). However, the results show that varying the lithosphere thickness affect the RSL response most, with the viscosity variations having less prominent effect. Incorporating global 3D variations of lithospheric thickness and upper and lower mantle viscosities reduces the RSL peak in the early Holocene by  $\sim 30$  m, while the RSL dip is reduced by only several meters.

It is important to note that the position and timing of the four index points make it impossible for a RSL curve to fit all four data points. None of the combinations of ice sheet model, viscoelastic Earth structure

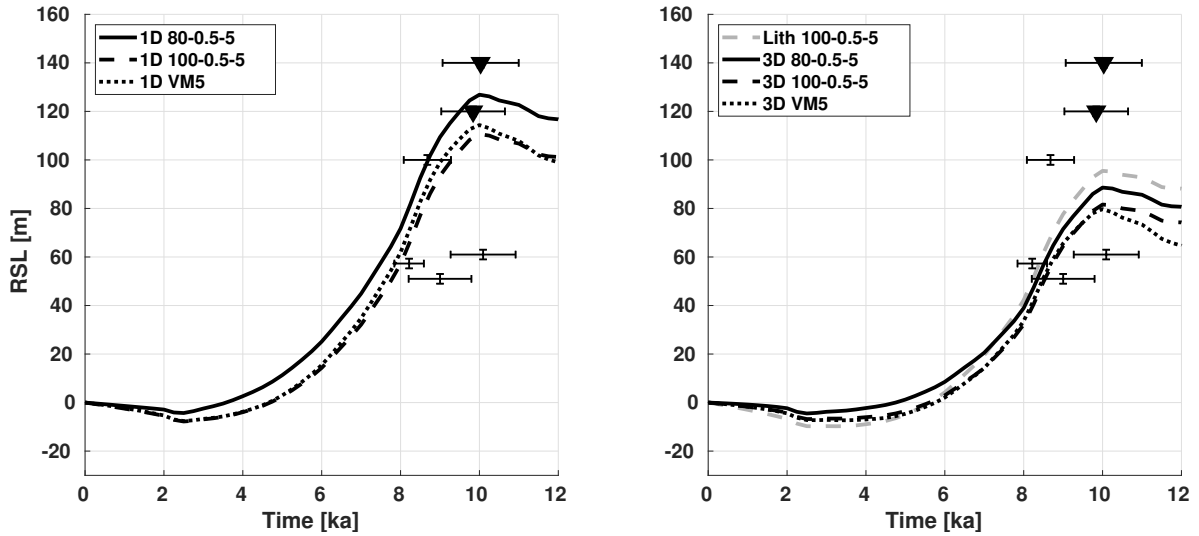


Figure 1.8: Modeled RSL curves due to GIA at Nuuk (64.48N, -50.99E), using 3D variations of solid the Earth parameters with ICE6G. Legend shows the configuration of the different simulation runs. The prefix 'Lith' means lithospheric thickness variations only.

and extent of ice margin retreat are therefore able to produce a RSL response with a shape and amplitude that fits all paleo RSL observations. It is worth noting that Huy3 is produced by fitting RSL responses to the three lower index points as well as the upper-limiting data. This provides an explanation for the good fit of the original Huy3 model with the lower three index points for almost all viscoelastic structures. The adapted Huy3 model shows a lower RSL response, thereby fitting the oldest two index points better but missing the most recent index point. On the other hand, ICE6G exhibits a better fit to the two most recent index points, though completely missing the oldest two index points due to the steep drop in RSL between 9 and 6 ka. The fit of the original ICE6G model with the two most recent index points provides the opportunity for the RSL curve to overpredict and therefore miss one or both of the upper-limiting data for most viscoelastic structures, especially for a thin lithosphere and a low upper mantle viscosity. For almost all viscoelastic structures, the adapted ICE6G model is consistent with the upper-limiting data and some of the RSL curves provide a fit with the three most recent RSL observations. Furthermore, the RSL curves from the 1D reference viscoelastic structures as well as the lithospheric thickness variation and full 3D variations each fit well with either the two most recent or the two lower index points.

Each combination of ice sheet model, viscoelastic Earth structure and ice margin chronology that provides a good fit of the RSL curve to at least two out of the four index points, while simultaneously remaining below the upper-limiting data, is deemed a set of modeling assumptions suitable for further evaluation.

#### 1.4.2 Modeled present-day RSL rates in Nuuk

Each combination of modeling assumptions describes a RSL curve with a specific contemporary RSL rate. Figure 1.9 shows the modeled results for the contemporary RSL rates due to GIA at the Nuuk tide gauge location (64.17N, -51.73E). The modeling assumptions that provide a good fit to the RSL observations as described in the previous section are indicated by a black plus-sign.

In general, the results illustrate that Huy3 provides a higher contemporary RSL rate than ICE6G for each combination of viscoelastic Earth structure and ice margin chronology. This is a result of the mechanisms described in Sections 1.3.1 and 1.4.1: 1) that the RSL dip in the late Holocene occurs later for Huy3 because

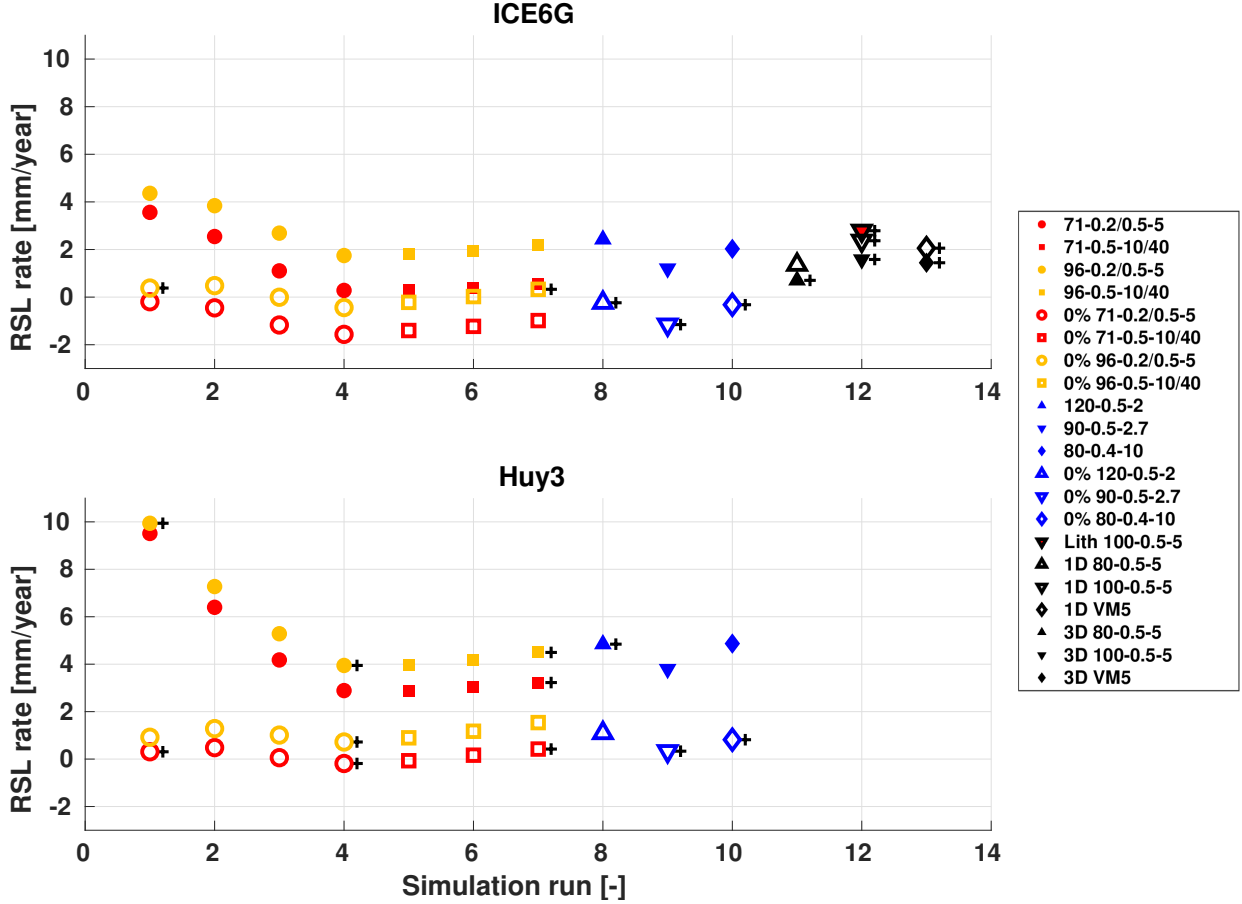


Figure 1.9: Modeled RSL rates due to GIA at Nuuk (64.17N, -51.73E), using ICE6G (top) and Huy3 (bottom). Different colored markers indicate different viscoelastic Earth structures. Example: 71-0.2/0.5-5 means lithosphere thickness of 71 km, upper mantle viscosity ranging from 0.2 to  $0.5 \cdot 10^{21}$  Pa·s and lower mantle viscosity of  $5 \cdot 10^{21}$  Pa·s. The prefix 0% denotes runs without ice margin retreat. The prefix Lith denotes only lithospheric thickness variations. The black plus-signs indicate model runs that provide a good fit to the paleo RSL observations.

the minimum extent of the ice margin is reached later, and 2) that Huy3 simulates the ice margin closer to Nuuk than ICE6G does, resulting in more pronounced gravitational and elastic effects. The magnitude and timing of the late-Holocene RSL dip directly dictates the contemporary RSL rate.

The results in Figure 1.9 show that increasing the upper mantle viscosity (red and orange dots from left to right) results in a significantly lower RSL rate. This corresponds well with the observation in Section 1.4.1 that a low upper mantle viscosity results in a high-amplitude RSL response with a large peak in the early Holocene and low dip in the late Holocene. Here, a lower dip results in a steeper present-day RSL curve, i.e. a higher contemporary RSL rate. This effect is more pronounced for Huy3, indicating that timing of the ice margin retreat and vicinity to the ice margin play an essential role in determining local RSL rate. Increasing the lower mantle viscosity (red and orange squares from left to right) results in a slightly higher RSL. This effect is less pronounced than the effect induced by varying the upper mantle viscosity, which corresponds to the previous observations of the RSL curves where a higher lower mantle viscosity mainly results in a slightly lower peak in the early Holocene. A thinner lithosphere generally results in a lower RSL rate for both ICE6G and Huy3 and for all viscosity values. However, the change in RSL rate is more pronounced for a higher upper mantle viscosity.

Omitting any ice margin retreat (prefix 0%) reduces the contemporary RSL rate, as can be observed by the difference between the filled and empty colored markers in Figure 1.9. A RSL rate reduction of 2-9  $\text{mmyr}^{-1}$  is observed when ice margin retreat is omitted, with the largest differences found for Huy3 with a low upper mantle viscosity. The RSL rate reduction is more pronounced for Huy3 than for ICE6G, again suggesting that the vicinity of Nuuk to the ice margin and the elastic and gravitational effects resulting from ice margin retreat play a significant role in determining the contemporary RSL rate.

Furthermore, using ICE6G and allowing for full 3D variations (filled black markers) of the viscoelastic Earth structure as opposed to their 1D reference values (empty black markers) results in a slightly lower RSL rate. Allowing for only lithospheric thickness variations (red-filled downward black triangle) results in a slightly higher RSL rate than for the 1D reference viscosity structure.

Model variation	Mean over all values	Mean only over good fits	Number of good fits
ICE6G	$1.94 \pm 1.24 \text{ mmyr}^{-1}$	N.A.	0
ICE6G (0% retreat)	$-0.48 \pm 0.65 \text{ mmyr}^{-1}$	$-0.20 \pm 0.62 \text{ mmyr}^{-1}$ (GIA3)	5
Huy3	$4.98 \pm 2.14 \text{ mmyr}^{-1}$	$5.29 \pm 2.67 \text{ mmyr}^{-1}$ (GIA1)	5
Huy3 (0% retreat)	$0.65 \pm 0.50 \text{ mmyr}^{-1}$	$0.40 \pm 0.36 \text{ mmyr}^{-1}$ (GIA2)	6
F3D (ICE6G)	$1.24 \pm 0.47 \text{ mmyr}^{-1}$	$1.24 \pm 0.47 \text{ mmyr}^{-1}$ (GIA4)	3
All	$1.75 \pm 2.37 \text{ mmyr}^{-1}$	$1.68 \pm 2.62 \text{ mmyr}^{-1}$ (GIA5)	19

Table 1.2: Mean and standard deviation ( $1\sigma$ ) for the RSL rates for ICE6G and Huy3, with and without ice margin retreat in Southwest Greenland and for the full 3D variations (ICE6G). The bottom row includes all model runs with all modeling assumptions. Means are calculated over all available runs per model variation and over all runs that provide a good fit with the paleo RSL observations.

Table 1.2 denotes the mean and standard deviation ( $1\sigma$ ) of the RSL rates for ICE6G and Huy3, with and without ice margin retreat, for the full 3D variations, and for all model runs. For each group, the mean is also calculated over only those model runs with viscoelastic Earth structures that provide a good fit (as defined above) to the paleo RSL observations, with the number of these model runs per group provided as well. It is clear that each model variation provides a significantly different mean RSL rate. Focusing only on model runs with good RSL observation fits shows that the RSL rate is substantially reduced (by  $4.89 \text{ mmyr}^{-1}$  for Huy3) when the ice margin is assumed to have not retreated past the present-day margin. No conclusion can be made on the effect of omission of ice margin retreat for ICE6G, as no good fits are available for the original ICE6G. Estimates of the RSL rate for ICE6G and Huy3 with no retreat and readvance overlap within their uncertainties. Five estimates of the contribution of GIA to the contemporary RSL rate are determined by grouping the model runs by their modeling assumptions. The estimates are shown in Table 1.2. Group 1 (GIA1) represents the best estimate while including full ice margin retreat as described by Huy3. Groups 2 and 3 (GIA2 and GIA3) represent the best estimates using Huy3 and ICE6G, respectively, while omitting any ice margin retreat. Group 4 (GIA4) represents the best estimate using ICE6G while incorporating global 3D variations of the viscoelastic Earth structure. Group 5 (GIA5) represents the best estimate while including all model runs that provide a good fit with the paleo RSL observations.

### Solid Earth deformation

Relative sea level is composed of both the local change in water distribution as well the local vertical land motion of the solid Earth. Decomposition of the RSL change allows me to evaluate the viscoelastic solid Earth deformation due to changes in ice and ocean mass loading since the LGM. Figure 1.10 shows the RSL

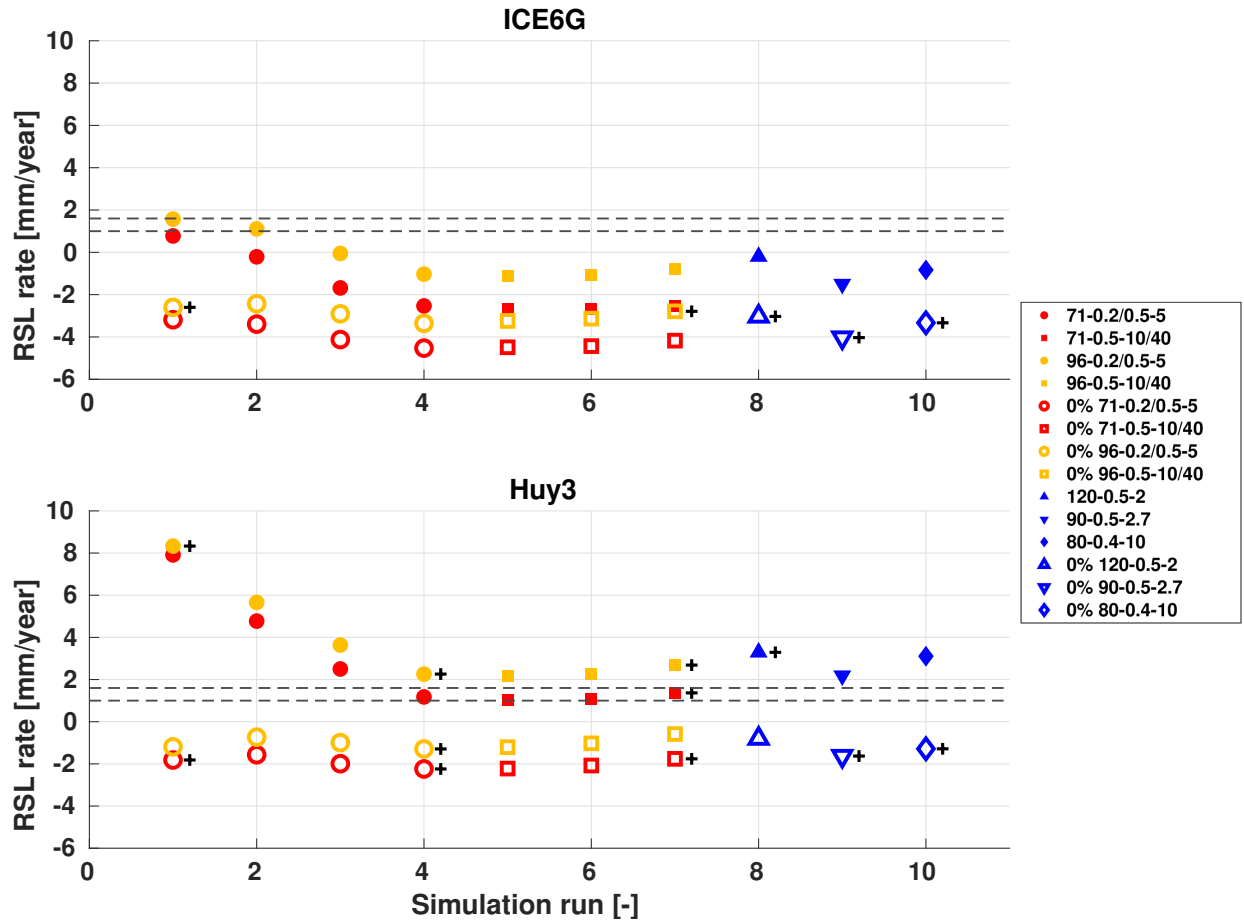


Figure 1.10: Modeled RSL rates due to GIA at Nuuk (64.17N, -51.73E), including only solid Earth deformation, using ICE6G (top) and Huy3 (bottom). Legend shows the configuration of the different simulation runs. Example: 71-0.2/0.5-5 means lithosphere thickness of 71km, upper mantle viscosity ranging from 0.2 to  $0.5 \cdot 10^{21}$  Pa-s and lower mantle viscosity of  $5 \cdot 10^{21}$  Pa-s. The prefix 0% means no ice margin retreat. Black plus signs indicate model runs with a good fit to the paleo RSL observations. Dashed lines indicate the  $1\sigma$  upper and lower range of the GIA rate ( $1.3 \pm 0.3$  mmyr $^{-1}$ ) at Nuuk found by Khan et al., 2016.

rate resulting from deformation of the solid Earth associated with GIA at Nuuk. Again, the combinations of ice sheet model, viscoelastic Earth structure and extent of ice margin retreat that provide a good fit to the paleo RSL observations are indicated by a black plus sign. The horizontal lines indicate the  $1\sigma$  upper and lower range of RSL rate due to viscoelastic solid Earth deformation rate from GIA at Nuuk ( $1.3 \pm 0.3$  mmyr $^{-1}$ ) as derived from measurements from the Greenland GPS Network (GNET) station in Nuuk (Khan et al., 2016). The results indicate that only some model runs of GIA1 provide a good match to the GPS-derived deformation rate. These runs have a lithospheric thickness of 71 km, an upper mantle viscosity of  $0.5 \cdot 10^{21}$  Pa-s and a lower mantle viscosity ranging from 5 to  $40 \cdot 10^{21}$  Pa-s. However, the other model runs in GIA1 overestimate the deformation rate. The mean deformation rate of GIA1 is  $3.59 \pm 2.74$  mmyr $^{-1}$ . GIA2 and GIA3 do not provide a good with with the GPS-derived deformation rate, with mean rates of  $-1.67 \pm 0.36$  mmyr $^{-1}$  and  $-3.16 \pm 0.56$  mmyr $^{-1}$ , respectively. No solid Earth deformation rate for GIA4 is available at this time. Khan et al., 2016 state that Huy3 and ICE5G are inconsistent with the GPS-inferred solid Earth deformation rate in Greenland, suggesting that the ice margin chronology and viscoelastic Earth structure may be incorrect. This is confirmed by the difference in the mean rate from GIA1 and mean rate from geodetic observations in Nuuk. This indicates that the magnitude of ice margin retreat described by Huy3 may be too large.

### 1.4.3 Tide gauge

Figure 1.11 shows the tide gauge records for the period 1958-2002, as well as for a more recent period 2014-2020. The tides as modeled with Tide Model Driver are subtracted to isolate the non-cyclical behaviour of the RSL. Figure 1.12 shows linear regressions of the tide gauge data with the modeled tides.

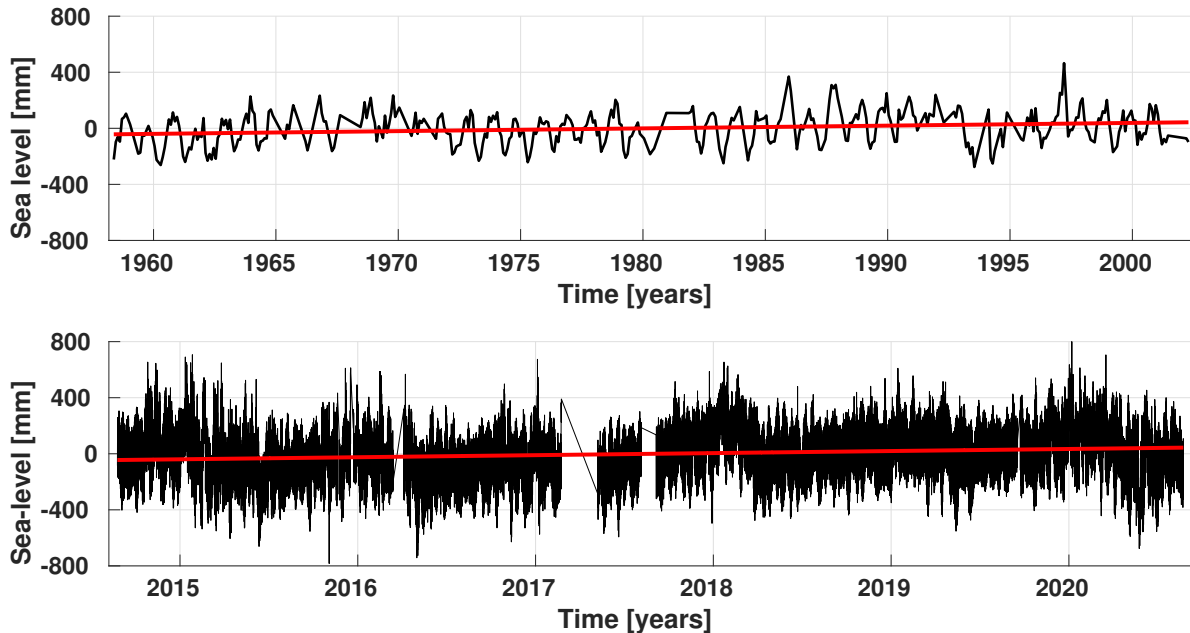


Figure 1.11: Time series of the tide gauge data at Nuuk for 1958-2002 (top) and 2014-2020 (bottom), with tides as modeled with TMD subtracted. Red lines are linear fits and represent RSL rates of  $1.95 \pm 0.89 \text{ mmyr}^{-1}$  for 1958-2002 and  $14.72 \pm 0.99 \text{ mmyr}^{-1}$  for 2014-2020.

While the data for 1958-2002 shows low correlation with the modeled tides ( $R^2 = 0.007$ ), the data for 2014-2020 shows an extremely high correlation ( $R^2 = 0.977$ ). This may be due to the frequency of the data in the records. Where 2014-2020 contains hourly data, 1958-2002 contains monthly averaged data, possibly inducing data-model misfits. A more proper fit for 1958-2002 could be achieved by utilizing the original hourly data. However, this data was not available. Linear fits are calculated through the data-model differences for both time periods, providing estimates of the RSL rates during these time periods. The calculated RSL rate for 1958-2002 is:

$$r_{58-02}^{OBS} = 1.95 \pm 0.89 \text{ mmyr}^{-1} \quad (1.2)$$

This corresponds well with the RSL rate of  $1.93 \pm 0.18 \text{ mmyr}^{-1}$  found by Spada et al., 2014 for the same record. The uncertainty found by the authors is lower as they used a more extensive method for determining the non-cyclical trend of the tide gauge record involving the Ensemble Empirical Mode Decomposition (Wu and Huang, 2009). For the period 2014-2020, the calculated RSL rate is:

$$r_{14-20}^{OBS} = 14.72 \pm 0.99 \text{ mmyr}^{-1} \quad (1.3)$$

Despite the plausibility of the significant increase in RSL rate found between 1958-2002 and 2014-2020 because of the evidence for accelerating sea level rise over the past decades (Oppenheimer et al., 2019), the value found for 2014-2020 is less robust than for the period 1958-2002. This is because the quality of the data is unknown and instrument drift may be present, possibly corrupting the data.

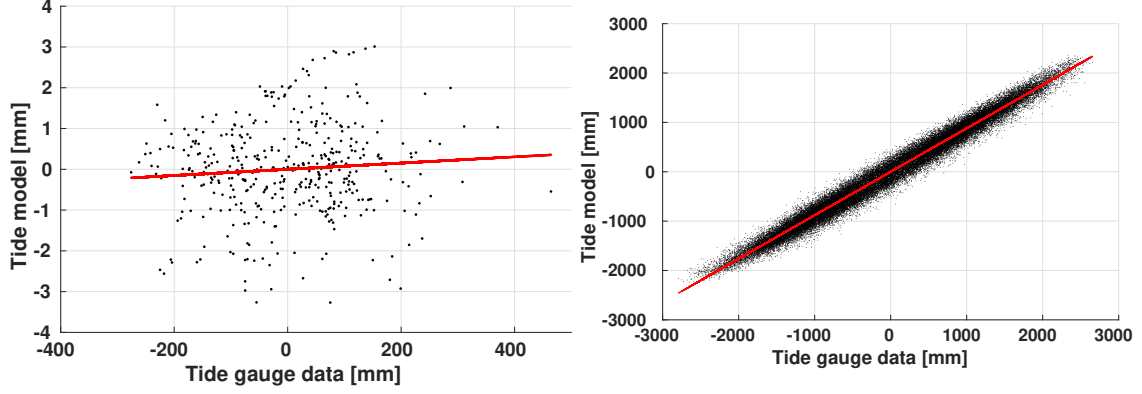


Figure 1.12: Linear regressions of tide gauge data with tide model data for 1958-2002 ( $R^2=0.007$ ) and 2014-2020 ( $R^2=0.977$ ).

#### 1.4.4 Literature analysis of RSL contributions

The modeled contributions of GIA to the RSL rate are augmented with the most current literature values for the remaining contributors (Greenland Ice Sheet (GrIS), Antarctic Ice Sheet (AIS), glaciers and ice caps, terrestrial water mass exchange and steric effects). The combined modeled and literature values provide an estimate for the total RSL in Nuuk and allows for comparison with the tide gauge-derived RSL rate. I rely here on work presented in the study by Spada et al., 2014. The authors of this study determined sea level fingerprint values at the Nuuk tide gauge location (64.17N, -51.73E) for the GrIS, AIS and glaciers and ice caps components of -5.5, 1.1 and 0.25, respectively. Sea level fingerprinting describes the spatial variability of global sea level change and can thus be used to translate global sea level change patterns to local patterns. The authors calculated the fingerprint values by solving the sea level equation using SELEN (DeGrandpre and Freymueller, 2019a).

The contribution of the GrIS to global RSL rate is determined from the sum of the contributions of: 1) the GrIS, and 2) the peripheral glaciers around the GrIS. A contribution  $0.20 \pm 0.05$  mmyr<sup>-1</sup> of the GrIS is found over 1958-2003 by analysis of aerial imagery (Kjeldsen et al., 2015). The peripheral glaciers around Greenland have contributed  $0.04 \pm 0.01$  mmyr<sup>-1</sup> over 1961-2006, determined by extrapolating glaciological and geodetic observations (Zemp et al., 2019). The periods over which the contribution to RSL rate for the GrIS and its peripheral glaciers are determined do not exactly match with the tide gauge period 1958-2002. However, as no data was found that does exactly match the tide gauge period, the values mentioned above are used in this analysis. A total contribution of the GrIS and its peripheral glaciers of  $0.24 \pm 0.04$  mmyr<sup>-1</sup> is calculated by adding both RSL rates and using error propagation. Combining the global RSL rate with the fingerprint value of -5.5 gives a RSL rate at Nuuk of:

$$r_{58-02}^{GrIS} = -5.5 \cdot [0.24 \pm 0.04] \text{ mmyr}^{-1} = -1.31 \pm 0.22 \text{ mmyr}^{-1}. \quad (1.4)$$

For the glaciers and ice caps contribution, a global RSL of  $13.97 \pm 11.70$  mm for the period 1961-2006 is given by Zemp et al., 2019. Again, this period almost completely matches the tide gauge period and is thus assumed acceptable for comparison with the tide gauge record. This contribution translates into a RSL rate of  $0.31 \pm 0.26$  mmyr<sup>-1</sup>, if a linear rate is assumed. Combining this value with the fingerprint value of 0.25 gives a RSL rate of:

$$r_{58-02}^{GIC} = 0.25 \cdot [0.31 \pm 0.26] \text{ mmyr}^{-1} = 0.08 \pm 0.07 \text{ mmyr}^{-1}. \quad (1.5)$$

For the AIS contribution, no updated values of the RSL rate are found. Therefore, similar to Spada et al., 2014, the contribution to the RSL rate of  $0.14 \pm 0.41$  mmyr<sup>-1</sup> as given by IPCC's Assessment Report 4

(AR4; IPCC, 2007) is used. Combined with the fingerprint value of 1.1, this gives:

$$r_{58-02}^{AIS} = 1.1 \cdot [0.14 \pm 0.41] \text{ mmyr}^{-1} = 0.15 \pm 0.45 \text{ mmyr}^{-1}. \quad (1.6)$$

The contribution to the RSL rate represented by terrestrial water mass exchange is taken from Spada et al., 2014, as no updated values of this component at Nuuk are found. The authors used values as provided by Slangen, 2012, who combined groundwater extraction data and reservoir impoundment data to determine the RSL rate due to terrestrial water mass exchange in the Davis Strait as:

$$r_{58-02}^{TER} = -0.07 \pm 0.07 \text{ mmyr}^{-1}. \quad (1.7)$$

Moreover, recent estimates of the global values for the contribution of terrestrial water mass exchange to the RSL rate of  $-0.12 \text{ mmyr}^{-1}$  for 1901-1990 and  $-0.07 \text{ mmyr}^{-1}$  for 1970-2015 are provided in IPCC's Special Report on the Ocean and Cryosphere in a Changing Climate (SROCC; Oppenheimer et al., 2019). These values are derived from coupled climate-hydrological model simulations (Wada et al., 2016) and are consistent with global rates of  $-0.20 \pm 0.20 \text{ mmyr}^{-1}$  for 1961-2003, found by Slangen, 2012. The contribution from terrestrial water mass exchange used in this study is thus assumed to be accurate.

For the steric contribution, the same value as found by Spada et al., 2014 is used. The authors obtained an estimate for the steric contribution to RSL by analyzing data from the National Oceanographic Data Center (NODC; <http://www.nodc.noaa.gov>). They used steric sea level anomalies between the ocean surface and 2000 m depth in the period between the pentads 1958-1062 and 2000-2005. The steric contribution at Nuuk is averaged over a  $3^\circ \times 3^\circ$  area centered around Nuuk and is estimated at:

$$r_{58-02}^{STE} = 0.39 \pm 0.14 \text{ mmyr}^{-1}. \quad (1.8)$$

No values for the contributions to the RSL rate of the GrIS, AIS, glaciers and ice caps, terrestrial water mass exchange and steric effects were found in previous studies that properly match with a more recent tide gauge record over the period 2014-2020. The GMSL acceleration has increased significantly over the past decades (Oppenheimer et al., 2019) and for a proper analysis of the modeled RSL rate due to GIA, and comparison with the tide gauge record, it is therefore essential to quantify the remaining contributors to the RSL rate over the exact tide gauge period to avoid errors. Despite the lack of values covering the 2014-2020 period, values covering a period several years earlier are available. From a synthesis combining published literature, expert assessment and statistical modeling, Bamber et al., 2018 determined values for the contribution to global sea level rise in 2012-2016 of  $0.68 \pm 0.04 \text{ mmyr}^{-1}$  for the GrIS, of  $0.63 \pm 0.08 \text{ mmyr}^{-1}$  for the glaciers and ice caps, and  $0.53 \pm 0.14 \text{ mmyr}^{-1}$  for the AIS. Using the fingerprint values provided by Spada et al., 2014, this translates into contributions at Nuuk of  $-3.74 \pm 0.22 \text{ mmyr}^{-1}$  for the GrIS,  $0.16 \pm 0.02 \text{ mmyr}^{-1}$  for the glaciers and ice caps, and  $0.58 \pm 0.15 \text{ mmyr}^{-1}$  for the AIS. An estimate for the global contribution from terrestrial water mass exchange of  $-0.21 \pm 0.15 \text{ mmyr}^{-1}$  is found for 2006-2015 by using ocean mass estimates from GRACE (Group, 2018). Purkey and Johnson, 2010 and Desbruyères et al., 2017 estimated a global contribution from steric effects of  $1.40 \pm 0.32 \text{ mmyr}^{-1}$  for 2006-2015 over the full ocean depth using Argo and repeat hydrography. The GIA component does not need to be revised for the 2014-2020 period as the GIA signal is assumed to be constant over the course of the two tide gauge periods.

The values for the contributions to RSL rate do not constitute a proper basis for comparison with the tide gauge record because the periods over which they are determined do not match well. However, a rough qualitative comparison of the most recent literature and tide gauge-derived estimates is possible. For the period 2012-2016, the contributions of the glaciers and ice caps and the AIS have doubled and quadrupled, respectively, since 1958-2002. Their contributions to the total RSL rate remain small however.

The contribution of the GrIS in 2012-2016 has almost tripled since 1958-2002, providing a significant negative contribution to the RSL rate at Nuuk. No comparison is available for the terrestrial water mass exchange and steric contributions at Nuuk. However, the global contribution of terrestrial water mass exchange has slightly decreased since 1958-2002, while the global contribution of steric effects more than tripled during this time. Summing these coarse estimates of the 21st century contributions to RSL rate at Nuuk suggests a lower total RSL rate than during the period 1958-2002, mainly due to the significant decrease of the GrIS contribution. This literature-based observation is in contrast with the significant increase in RSL rate found for the 2014-2020 tide gauge record. This difference suggests that either the literature-based estimates mentioned above are inaccurate or that the contribution of each estimate during 2014-2020 is significantly different than their contributions during the periods mentioned above. It may also suggest that the tide gauge-derived RSL rate is not accurate, possibly due to instrument drift.

#### 1.4.5 Comparison of RSL rates

The individual contributions of the RSL rate during 1958-2002 are added and combined with each of the five GIA contributions (GIA1-GIA5), constituting five estimates for the total RSL rate (TOT1-TOT5) at Nuuk during the period 1958-2002. Figure 1.13 shows the literature-based contributions (black), modeled GIA contributions (blue), total RSL rates (red) and the tide gauge-derived RSL rate (orange).

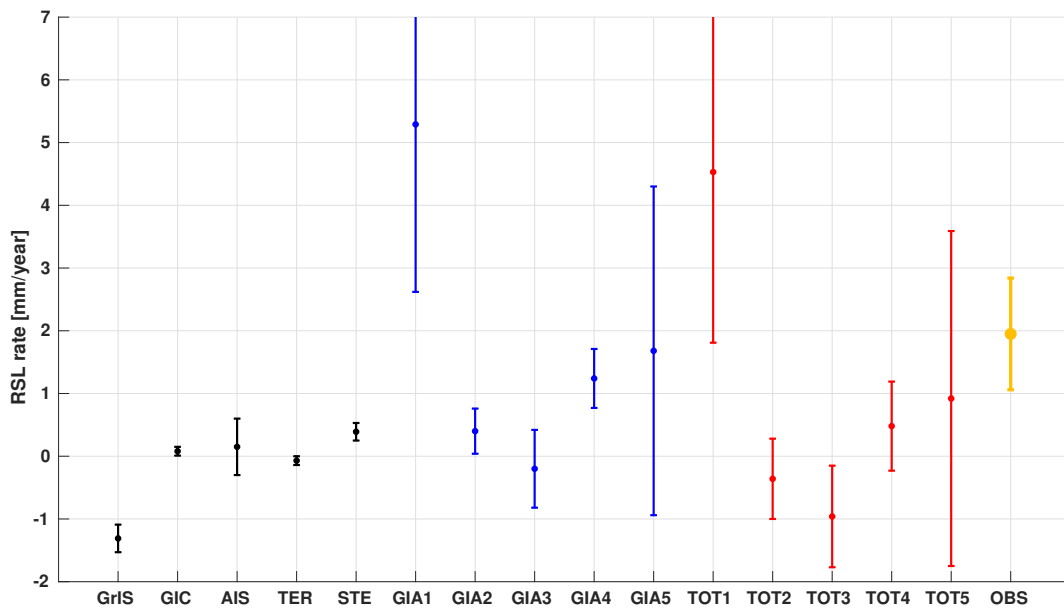


Figure 1.13: Comparison of the modeling- and literature-based RSL rate at Nuuk (64.17N, -51.73E) for 1958-2002 with the tide gauge-derived RSL rate (orange). The contributions from the literature-based GrIS, GIC, AIS, TER and STE (black) are combined with the five modeled contributions from (GIA1-GIA5; blue), providing five estimates for the total RSL rate (TOT1-TOT5; red).

The contributions of the glaciers and ice caps, AIS and terrestrial water mass exchange components are relatively small and thus play only a minor role. However, the uncertainty of the AIS is relatively large, adding to the uncertainty of the total RSL rate. It is apparent that the GrIS is responsible for the largest literature-based contribution. Its contribution is strongly negative (RSL drop), as is expected from the theory of elastic deformation and gravitational effects in response a decreasing local ice mass load.

All GIA contributions show significant differences in magnitude as well as uncertainty. Especially GIA1 and

GIA5 show high uncertainty, which is due to the inclusion of the extremely high RSL rate for low upper mantle viscosity (96p25) when using Huy3 (Figure 1.9). The high value for GIA1 may be a result of the ice margin retreat and readvance described by Huy3. The ice margin is modeled consistently  $\sim 100$  km closer to Nuuk over the past 7 ka by Huy3 than by ICE6G. Ice mass loading changes have a significant local effect on the RSL. Consequently, a location difference in ice margin chronology of this magnitude may result in a significant difference in GIA rate. All GIA contributions, except GIA3, show a RSL rise and thus counteract the negative RSL rate contribution from the GrIS. A positive contribution to the GIA rate is expected from the subsiding peripheral bulge of the LIS on which Nuuk is located. Moreover, assuming late-Holocene ice margin readvance around Nuuk gives rise to contemporary subsidence due to increased ice mass loading, adding to the RSL rise in this region. For GIA2 and GIA3, no ice margin retreat is assumed and therefore no subsidence due to an increase in local ice mass loading is modeled, explaining the lower rates for GIA2 and GIA3. The contribution from GIA4 shows an intermediate value (between GIA1 and GIA2/3) of the GIA rate. For GIA4, global 3D variations of the viscoelastic Earth structure are used with ICE6G. The ice margin chronology of ICE6G includes ice margin retreat and readvance at a larger distance from Nuuk than modeled by Huy3. This decreases the subsidence effects in response to the increasing late-Holocene ice mass loading, resulting in the intermediate GIA rate. The value for GIA4 corresponds best with the GIA rate found by Spada et al., 2014, who modeled GIA rates of 0.81 and 0.64  $\text{mmyr}^{-1}$ , using ICE5G and viscoelastic structures of 90-0.5-2.7 and 80-0.4-10, respectively. These values are obtained by assuming mantle compressibility, which is accounted for in the GIA model used in this study as well. GIA5 shows a slightly higher value than GIA4 as it includes model runs from all model variations that fit well with the paleo RSL observations (Figure 1.7).

The total RSL rates are calculated by adding the mean rates of each contribution and using error propagation. Assuming the late-Holocene ice margin retreat and readvance from Huy3 results in an overestimation of the RSL rate (TOT1) compared to the observed RSL rate. This suggests that one or more of the literature-based contributions is not correct. The contribution of the GrIS has the highest fingerprint value at Nuuk, it is therefore most sensitive to a change in contribution to the global sea level. Since the fingerprint value for the GrIS is negative and a lower total RSL rate is necessary to match the observed RSL rate, a higher mass loss rate for the GrIS is required than suggested by Kjeldsen et al., 2015 and Zemp et al., 2019. However, it is more likely that the overestimation of TOT1 compared to the observed RSL rate suggests that the magnitude of the ice margin retreat in Southwest Greenland in Huy3 may be too large. It may also be possible that the ice thickness of the LIS during the LGM is too large. Assuming no ice margin retreat and readvance, using both ICE6G and Huy3, results in an underestimation of the RSL rate (TOT2 and TOT3). This suggests that one or more of the literature-based contributions may be incorrect. In particular, a lower-magnitude contribution of the GrIS is required to match TOT2 and TOT3 with the observed RSL rate. Recalling the negative fingerprint value for the GrIS at Nuuk, this would require a lower mass loss rate from the GrIS than suggested by Kjeldsen et al., 2015 and Zemp et al., 2019. More likely is that the underestimation of TOT2 and TOT3 suggests that at least some degree of ice margin retreat and readvance in Southwest Greenland is necessary to provide a good match with the observed RSL rate. Assuming global 3D variations (TOT4) and using ICE6G with ice margin retreat, the total RSL rate is only slightly underestimated. This misfit suggests that the mass loss from the GrIS may be slightly smaller than suggested. It is apparent that TOT5 corresponds best with the observed RSL rate. As TOT5 includes all model runs, with (8 runs) and without (11 runs) ice margin retreat, it roughly represents an intermediate ice margin retreat. This suggests that model variations with an intermediate degree of ice margin retreat may provide the best fit with the observed RSL rate. Overall, a difference in RSL rate of 0.92-2.58  $\text{mmyr}^{-1}$  is found between the modeling- and literature-based estimates and the observed estimate. No conclusions can be made from this analysis about the most plausible viscoelastic Earth structure, globally nor around Greenland. However, including

the range of viscoelastic Earth structures that fit well with the paleo RSL observations provides a means of isolating the effect of ice margin chronology on the RSL rate.

The differences in RSL rates could be induced by inaccurate values from literature, modeling or instrumentation. In the case of the literature values, not all contributions are determined over the exact same period, giving rise to possible errors. Moreover, as the contribution from the GrIS has the largest effect around Nuuk, inaccuracies from literature are most likely to originate from the estimate of the Greenland ice sheet mass balance. As the GIA contributions have the largest values and uncertainties, inaccuracies in the total RSL rate are most likely to originate from this component. Representation of ice margin chronology is a significant driver of the RSL rate around Nuuk, especially the representation of the Southwest GrIS and, to a lesser extent, the LIS during the Holocene. These may therefore constitute a significant fraction of the misfit. Moreover, uncertainties in and lack of constraints of the viscoelastic Earth structure globally and around Greenland may also give rise to the misfit in total RSL rate. Furthermore, sediment compaction is not accounted for in the GIA model used in this study. However, Ferrier et al., 2017 suggest that minor sea level changes are observed if sediment compaction is accounted for when solving the SLE. Including sediment compaction may thus provide a more realistic modeled GIA rate, though no significant changes are expected. A similar RSL rate is determined from the same 1958-2002 tide gauge record by Spada et al., 2014, who use a different approach for calculating the RSL rate than the approach used in this study. However, systematic errors of the tide gauge instrumentation may be present in the record and may give rise to an inaccurate estimate of the RSL rate. Moreover, the completeness of the tide gauge record is only 76%. This lack of data may induce an error in the linear fit that determines the RSL rate.

## 1.5 Conclusion

In this thesis I investigated the sensitivity of the GrIS to warming during the Holocene, specifically the late-Holocene ice margin retreat and readvance in Southwest Greenland. I also evaluated the implications this ice sheet evolution has for our interpretation of contemporary melt of the GrIS. I modeled the contribution of GIA to the contemporary RSL rate at Nuuk in Southwest Greenland and augmented this with literature-based estimates for the remaining contributions to RSL rate to obtain estimates for the total RSL rate for the period 1958-2002. I compared this modeling- and literature-based RSL rate with a tide gauge-derived RSL rate at the same location and period. In my analysis I included a range of 1D and 3D viscoelastic Earth structures and two ice sheet models, ICE6G and Huy3. The ice sheet models are utilized in their original form as well as in an altered form in which late-Holocene ice margin retreat in Southwest Greenland is omitted. As a means of determining significance, I only include model runs in my analysis that provide a fit to at least two out of the four index paleo sea level observations in Nuuk, while remaining below the two upper-limiting data.

The results from my analysis show an overestimation of present-day RSL rate in Nuuk for the original Huy3 ice sheet model compared to the tide gauge-derived present-day RSL rate. Moreover, the results show an overestimation of present-day viscoelastic solid Earth deformation rate in Nuuk for the original Huy3 ice sheet model compared to the GPS-derived deformation rate. The overestimations most likely originate from the modeled estimate of the GIA contribution to the total RSL rate. The results suggest that the ice margin chronology in Southwest Greenland modeled by Huy3 may be incorrect, indicating that either the timing of the ice margin retreat is incorrect or that the magnitude of the ice margin retreat is too large. Furthermore, the results from my analysis show an underestimation of present-day RSL rate in Nuuk for the altered ICE6G and Huy3 models in which ice margin retreat in Southwest Greenland is omitted, indicating that some degree of late-Holocene ice margin retreat in Southwest Greenland is necessary. However, the degree of ice margin retreat might be smaller than what has been suggested by Huy3.

## 2 The role of bare ice extent and albedo variability on runoff from the Greenland Ice Sheet

### Abstract

Mass loss from the Greenland ice sheet (GrIS) has accelerated over the past decades, mainly due to enhanced surface melting and liquid water runoff in response to atmospheric warming. The majority of runoff from the GrIS originates from exposure of the darker bare ice in the ablation zone. Since surface albedo plays a critical role in modulating surface melt, it is imperative to understand the processes governing albedo variability to accurately project future mass loss from the GrIS. Bare ice albedo is spatio-temporally variable and contingent on non-linear feedbacks and presence of surface-darkening impurities. Due to lack of understanding of these processes, the full extent of bare ice albedo variability can not yet be represented properly in climate models. In this study, I compare output from the Modèle Atmosphérique Régional (MAR), a regional climate model, with satellite imagery from the Moderate Resolution Imaging Spectroradiometer (MODIS), focusing on bare ice extent and albedo. The findings suggest that MAR overestimates bare ice albedo by  $\sim 0.05$  on average during 2000-2018, with respect to the observed bare ice albedo. This bare ice albedo bias results in an underestimation of total runoff over the entire GrIS of 128 Gton during 2000-2018, or  $\sim 7$  Gton year<sup>-1</sup>.

## 2.1 Introduction

Global mean sea level (GMSL) rise has significantly accelerated over the past decades (Chen et al., 2017). While many coastal-based communities experience a real and increasing risk of flooding, it remains unclear exactly how fast the sea level will rise and how the contribution of each source will evolve in the future (Kopp et al., 2017). The ice mass loss from the Greenland Ice Sheet (GrIS) is currently one of the largest contributors to GMSL rise (11-24%, Kjeldsen et al., 2015) and will continue to be so by the end of this century (Rignot et al., 2011). According to (Church et al., 2013), the GrIS' contribution will constitute of 15-20% of GMSL by 2081-2100. To better constrain projections of the future contribution of the GrIS it is imperative to improve model representation of physical processes responsible for ice mass loss. Evaluation of climate model output with observational data can provide insight in the model's ability to represent the physical processes at play and can subsequently highlight regions for model improvement (Broeke et al., 2017). In this thesis I will focus on evaluating the performance of Modèle Atmosphérique Régional (MAR), a regional climate model, by comparing its output with satellite imagery from Moderate Resolution Imaging Spectroradiometer (MODIS). I will focus on the representation of the bare ice zone, which is currently responsible for the majority of runoff from the GrIS (Steger et al., 2017).

Greenland's total mass loss for 2000-2018 originated for 55% from a reduced surface mass balance and for 45% from enhanced ice discharge from outlet glaciers (Mouginot et al., 2019). The decrease in surface mass balance is driven primarily by an increase in melt and subsequent liquid water runoff in response to recent atmospheric warming (Broeke et al., 2017). Melt and runoff are in part controlled by albedo, a parameter describing the amount of solar energy that is reflected, or alternatively, absorbed. Low albedo surfaces, such as bare ice, absorb more radiation which is subsequently transformed to heat, resulting in melt. The bare ice zone encompasses only a small fraction of the GrIS, along the margins of the ice sheet, where the rest of the ice sheet is mostly and perpetually covered by snow or firn. However, since bare ice is darker than snow it is responsible for the majority of melt and runoff from the GrIS. In the period 1960-2014, bare ice was responsible for  $\sim 78\%$  of the runoff from the GrIS (Steger et al., 2017).

Despite the significance of bare ice to runoff from the GrIS, representation of bare ice albedo in climate models, such as MAR, is complicated. Bare ice albedo is spatio-temporally variable in response to non-linear positive feedbacks between absorbed shortwave radiation and surface melt (Box et al., 2012 and Ryan et al., 2019). Furthermore, bare ice exposure and meltwater production induce exposure of dust and cryoconite (Tedstone et al., 2017) and the production of ice algal blooms (Wang et al., 2018). These light-absorbing impurities reduce the bare ice albedo, further enhancing meltwater production and runoff. The difficulty in representing bare ice albedo in climate models partly originates from a lack of understanding of these processes governing bare ice and melt and may result in a reduced accuracy of runoff projections (Alexander et al., 2014).

In this thesis I will evaluate the performance of the regional climate model MAR with respect to bare ice extent, bare ice albedo and runoff. I will compare output from MAR with satellite imagery from MODIS during the summer months June, July and August in 2000-2018. Furthermore, I will include MAR output on different horizontal resolutions and climate forcings to investigate their effects on the correlation between MAR and MODIS. As a last step, I will utilize an energy balance model (Pellicciotti et al., 2005) to analyze the effect of a bias in bare ice albedo, as modelled by MAR and as observed by MODIS, on estimates of runoff.

## 2.2 Background

### 2.2.1 Greenland Ice Sheet mass balance

Ice mass loss from the GrIS is controlled by ice dynamics and by surface mass balance. The ice on the GrIS continuously flows under its own weight towards the margins of the ice sheet, i.e. ice dynamics. At the margins, marine-terminating glaciers exist, providing an outlet for ice flow and mass discharge through calving of the glacier termini into the surrounding oceans. Mass loss through ice dynamics also includes ice mass loss due to basal melt when the ice sheet flows over the grounding line, the point at which the glacier detaches from the bed rock and starts to float in the ocean. Surface mass balance (SMB) refers to the balance over the entire ice sheet between accumulation (SMB > 0) and ablation (SMB < 0), according to:

$$SMB = SF + RF - R - SU - EV - ER. \quad (2.1)$$

Here, accumulation is defined as the sum of all positive fluxes to the surface mass of the GrIS, i.e. precipitation in the form of snowfall and rainfall (SF and RF). Ablation is defined as the sum of all negative fluxes to the mass on the surface of the GrIS, i.e. runoff (R) from melt of ice and snow, sublimation (SU), evaporation (EV) and erosion (ER) Broeke et al., 2017. The equilibrium line altitude denotes the boundary between the accumulation zone at higher elevations and the ablation zone at lower elevations.

Between 1972 and 2018, the total mass loss from the GrIS was dominated for  $66 \pm 8\%$  by ice dynamics, amounting to a total of  $9.1 \pm 0.3$  mm of GMSL rise. The contribution from SMB was thus only  $34 \pm 8\%$  to the total mass loss from the GrIS, or  $4.6 \pm 1.0$  mm of GMSL, during this period. Most of the mass loss in 1972-2018 originated from the Northwestern and Southeastern GrIS through ice dynamics, as these regions are home to many of Greenland’s marine-terminating glaciers. However, a more recent study by Shepherd et al., 2020 suggests that in the period 1992-2018 50.3% of the mass loss is attributable to a decreased SMB, indicating the significant increase in importance of SMB to GrIS ice mass loss. The remaining 49.7% of the mass loss is due to ice dynamics. The total GMSL caused by both processes amounts to  $10.8 \pm 0.9$  mm. In the period 2010-2018 the Southwestern GrIS contributed -41 Gton/yr to the decrease in SMB (Mouginot et al., 2019), making it the largest present-day contributor to ice mass loss through SMB on the GrIS (Shepherd et al., 2020).

The recent decrease in surface mass balance is driven primarily by an increase in melt and runoff in response to atmospheric warming. A recent summer warming of about  $\sim 2$  °C is observed around Greenland since the early 1990s (Hanna et al., 2012 and Box, 2013). This has increased runoff by 40%, while precipitation, sublimation and erosion changes since the early 1990s are not significant (Broeke et al., 2016 and Broeke et al., 2017). The recent increasing temperatures and subsequent changes in runoff are suggested to originate from recent changes in atmospheric conditions around Greenland (Hanna et al., 2014). Increased frequency of persistent anticyclonic conditions over Greenland are favorable for atmospheric blocking and explain most of the recent increase in surface melt (Fettweis et al., 2013 and Tedesco et al., 2016b). Hanna et al., 2018 and McLeod and Mote, 2015 suggest that a significant increase in high summer pressure blocking over Greenland (Greenland Blocking Index) since the 1990s, indicated by a negative trend in the North Atlantic Oscillation index (Hanna et al., 2015), is a major driver of the recent increase in surface melt on the GrIS.

### 2.2.2 Bare ice and albedo feedbacks

A large portion of runoff is produced through melt in the bare ice zone, which lies in the ablation zone along the margins of the GrIS (Figure 2.1). Bare ice is seasonally exposed when the overlying snow and firn

melt in response to the higher summer temperatures and increased summer solar radiation in response to a decreased solar zenith angle. Albedo is an essential regulator of absorption of incoming solar radiation. Dark surfaces, such as bare ice, absorb more radiation, which is transformed to heat, resulting in melt. Bare ice is therefore an important contributor to the overall absorption of incoming solar radiation and the total melt on the GrIS.

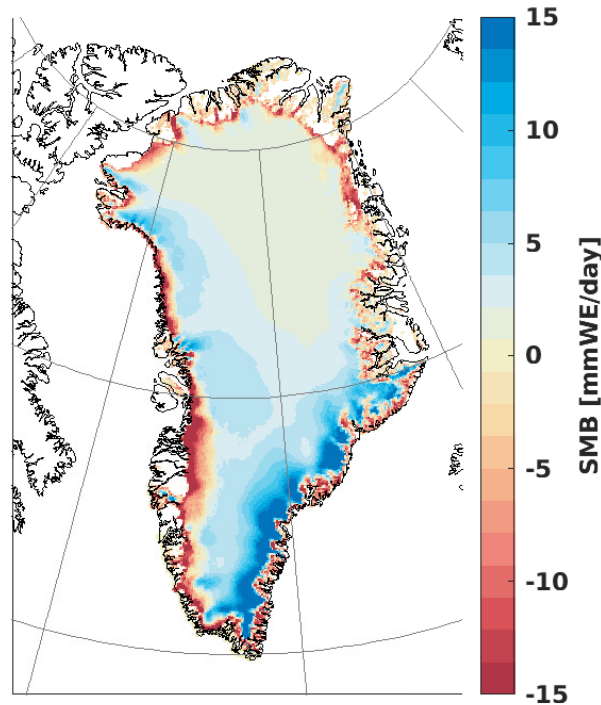


Figure 2.1: Average SMB over the entire year in 2000-2018 as modelled by MAR. Ablation zone is represented by the orange and red areas, the accumulation zone is represented by the blue areas.

In all stages of summer surface metamorphism, positive feedbacks occur. Bare ice extent as well as bare ice albedo impart non-linear positive feedbacks between absorbed shortwave radiation and surface melt. Through an increase in absorbed shortwave radiation during summer, snow melts, increasing bare ice extent. As the snowline, the boundary between ice and snow, migrates upwards, the underlying darker bare ice is exposed. This process reduces the overall GrIS albedo, further inducing more absorption of shortwave radiation. This is termed the snowline-albedo feedback (Ryan et al., 2019). Synchronously, the snow melt-albedo feedback plays an essential role in the ablation zone (Jakobs et al., 2019). Melted snow may refreeze in the colder snowpack, producing snow grains ten times the size of grains that have merely been subjected to dry compaction ( $\sim 1$  mm vs.  $\sim 0.1$  mm). A reduction of photonic backscatter in the snowpack is observed for larger snow grains, which decreases albedo and increases absorption of solar radiation and melt (Gardner and Sharp, 2010). Moreover, an increase in absorbed shortwave radiation during summer results in enhanced surface meltwater production in the bare ice zone, with water having a significantly lower albedo than bare ice. The presence of meltwater thus reduces the albedo in the bare ice zone, further increasing absorption of shortwave radiation. This process is termed the bare ice-albedo feedback. Moreover, melt in the bare ice zone induces exposure, accumulation and production of light-absorbing impurities on ice, further darkening the albedo. High amounts of light-absorbing impurities from a range of sources are present in the bare ice zone (Tedesco et al., 2016a and Tedstone et al., 2017). For instance, Wientjes et al., 2012 suggest that

outcropping ice layers reveal dust on the surface that is darker than the surrounding ice. These dust layers were deposited in the accumulation zone during the late Holocene and were transported to the lower ablation zone through ice flow. In addition to dust, accumulation of cryoconite can darken the bare ice surface. The darker cryoconite absorbs more shortwave radiation and subsequently produces more meltwater, giving rise to development of quasi-cylindrical cryoconite holes (Cook et al., 2016). These cryoconite holes range from centimeters to meters in depth and diameter (MacDonell and Fitzsimons, 2008) and are filled with meltwater, lowering the albedo in the bare ice zone. Furthermore, Wang et al., 2018 found an abundant presence of supraglacial ice algal blooms in the bare ice zone in the Southwestern GrIS, with a significant correlation between dust content and microbial abundance revealed by Stibal et al., 2017. Ice algal blooms are suggested to significantly lower the albedo of the bare ice zone, further enhancing meltwater production and runoff (Williamson et al., 2018, Williamson et al., 2020 and Cook et al., 2020).

### 2.3 Method

In this thesis I will evaluate the performance of the regional climate model MAR with respect to bare ice extent, bare ice albedo and runoff. I use MARv3.11.2, a regional climate model commonly used for projections of SMB on Greenland (Fettweis et al., 2017). Daily output of MAR is used on its native oblique stereographic projection. In my analysis I include MAR output forced with: 1) ERA5 (Hersbach et al., 2020), produced by the European Centre for Medium-Range Weather Forecasts (ECMWF) on horizontal model resolutions of 7.5, 10, 15 and 20 km for MAR; and 2) NCEP/NCAR-Reanalysis 1 (hereafter referred to as NCEP1; Kalnay et al., 1996), produced as a joint product from the National Centers for Environmental Prediction (NCEP) and the National Center for Atmospheric Research (NCAR) on a horizontal model resolution of 20 km for MAR.

I will compare the output from MAR with satellite imagery from MODIS on board NASA's Terra satellite. I use the MOD09GA Version 6 daily spectral surface reflectance data, mosaiced and reprojected onto a sinusoidal grid of 500 m horizontal resolution. Corrections have already been applied to this product for atmospheric conditions such as aerosols, gasses and Rayleigh scattering. However, the MOD09GA Version 6 product may erroneously detect retrievals as a high aerosol over bright surfaces and at large viewing angles (Vermote, 2015). I use the cloud mask from the MOD10A1 Version 6 daily snow cover product to remove clouds from the MOD09GA product. Moreover, the MOD10A1 product contains daily albedo values over the entire GrIS (Hall and Riggs, 2016). Similar to the reflectance data, the MOD10A1 product is mosaiced and reprojected onto a sinusoidal grid of 500 m horizontal resolution. The MOD10A1 product albedo values may be positively biased above a latitude of  $70^\circ$  due to viewing geometry and large solar zenith angle (Alexander et al., 2014).

The study period consists of the summer months June, July and August (JJA) from 2000 to 2018. This study period is chosen to accommodate the observation period of MODIS and the annual season of bare ice exposure on the GrIS, when surface albedo has the largest impact on SMB (Alexander et al., 2014). Furthermore, MODIS data are found to be less reliable outside JJA (Stroeve et al., 2006 and Box et al., 2012). In my analysis I will include output from MAR forced with different climate reanalyses on different horizontal resolutions. The range of climate forcings and resolutions used in this analysis can provide insight in their effects on the correlation between MAR and MODIS. In the final section of this thesis I will use an energy balance model (Pellicciotti et al., 2005) to analyse the effect of a bias in bare ice albedo, between MAR and MODIS, on estimates of runoff as modelled by MAR.

### 2.3.1 ELA estimate

A long-term average equilibrium line altitude (ELA) over 2000-2018 is determined from the SMB output from MAR. Daily SMB values during JJA over 2000-2018 are summed for each cell on the entire GrIS, creating a long-term summer average accumulation and ablation zone. All cells in the ablation zone are ordered according to their elevation values. The long-term average summer ELA is estimated at 1624 m, as the 95th percentile of the ordered elevation values. This ensures omission of sporadically high ablation cell detections and provides a conservative estimate.

### 2.3.2 Bare ice extent

#### MAR

Bare ice pixels are constrained to those pixels within the boundaries of the MAR ice sheet mask and below the long-term average ELA. Moreover, the variables from MAR representing snowpack height and density are used to discern between cells containing bare ice or snow on the surface. The variable snowpack height represents the thickness of the snow layer over the ice sheet and an upper threshold of 0 m is used to exclude cells containing snow. According to Alexander et al., 2014, MAR simulates bare ice with a density between 920 and 925 kg/m<sup>3</sup>. These values are therefore used as lower and upper thresholds, eliminating any cells with a density outside this range. The annual maximum bare ice extent is defined as the area covered by those pixels that are detected to be bare ice at least once during JJA in one year.

#### MODIS

The MOD09GA product and a digital elevation model of the GrIS as described by Bamber et al., 2001 is used to define the satellite-derived extent and elevation of the GrIS. Removed clouds from the MOD09GA product are assumed to be snow to determine a conservative estimate of the bare ice extent. Figure 2.2 shows the cloud cover for 9 July 2012 to illustrate that clouds may obstruct view of the ablation zone, and thus potentially mask bare ice. The bare ice extent on the GrIS is extracted by applying an upper threshold of 0.6 to the 841-876 nm band, the remaining pixels on the GrIS are defined as snow. A lower boundary of the MODIS-derived annual maximum bare ice extent is composed of those pixels below the long-term average ELA that are detected to be bare ice for a minimum of 10% of the observed days in JJA. This provides a conservative estimate and ensures the omission of sporadic and erroneous bare ice detections by MODIS such as meltwater lakes and streams. An upper boundary of the annual maximum bare ice extent is composed of the detected bare ice pixels with an addition of those pixels that are detected to be clouds for a minimum of 90% of the observed days in JJA. Because, if pixels are cloud-covered for more than 90% of the days, detection of bare ice for more than 10% of the days is not possible.

### 2.3.3 Albedo

The performance of MAR in modelling bare ice albedo is evaluated on the overlapping bare ice extent as modelled by MAR and as observed with MODIS. The MOD09GA and MOD10A1 data is reprojected and resampled onto the same projection and resolution as MAR to determine, on a pixel-by-pixel basis, for each day in JJA in 2000-2018, the overlapping bare ice extent. The albedo from MAR and from MODIS is compared on this overlapping bare ice extent. Modelled albedo values are directly taken from MAR output, which contains daily albedo values over the entire GrIS. The bare ice albedo scheme in MARv2 existed of simply assigning a fixed value of 0.45 to bare ice albedo. The improved MARv3 determines bare ice albedo as a function of accumulated surface water height and slope of the ice sheet, following an exponential relation between pure bare ice albedo and water albedo. MAR includes lower and upper boundaries for the bare ice albedo of 0.4 and 0.55. However, lower bare ice albedo values between 0.2 and 0.4 have been observed

using MODIS (Navari et al., 2018) and by some PROMICE automatic weather stations (Tedesco et al., 2016a). These low albedo values are a result of impurities on the ice, which are not taken into account in the MARv3 bare ice albedo scheme. The albedo values for MODIS are taken from the MOD10A1 product, which contains daily albedo values for the entire GrIS.

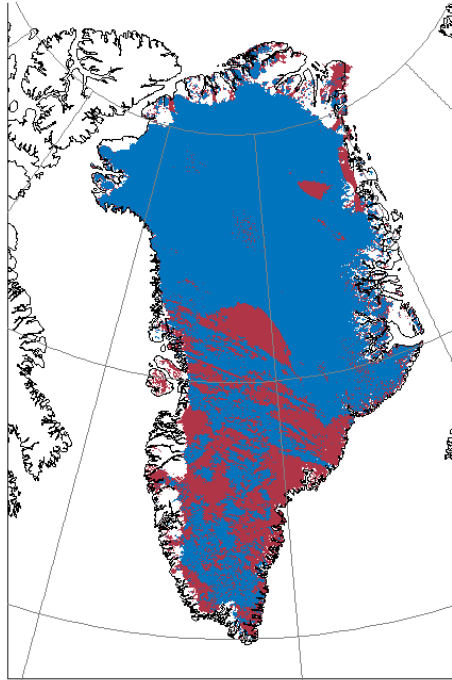


Figure 2.2: Example of cloud cover on 9 July 2012 from the MOD10A1 product. Blue and red denote ice sheet and cloud cover, respectively.

### 2.3.4 Runoff

Assuming a potential bias in bare ice albedo, on the one hand modelled by MAR and on the other hand observed with MODIS, I will determine the effect of this albedo bias on estimates of runoff by MAR. I will use an energy balance model as described by Pellicciotti et al., 2005 in which runoff is defined as a function of temperature, albedo and incoming shortwave radiation, according to:

$$R = a \cdot T + b \cdot (1 - \alpha) \cdot SW_{in}. \quad (2.2)$$

Here,  $R$  [ $\text{mmWEday}^{-1}$ ] represents runoff,  $T$  [ $^{\circ}\text{C}$ ] is temperature,  $\alpha$  is albedo  $[-]$ ,  $SW_{in}$  [ $\text{Wm}^{-2}$ ] is incoming shortwave radiation, and  $a$  [ $\text{mm}^{\circ}\text{C}^{-1}\text{day}^{-1}$ ] and  $b$  [ $\text{m}^2\text{mmW}^{-1}\text{day}^{-1}$ ] are empirical coefficients representing, respectively, the temperature factor and the shortwave radiation factor. To determine the difference in runoff,  $\Delta R$ , only due to a bias in albedo, I use the same temperature and incoming shortwave radiation (taken from MAR) for both MAR and MODIS, resulting in:

$$\Delta R = R_{MAR} - R_{MODIS} \quad (2.3)$$

$$\Delta R = a \cdot (T_{MAR} - T_{MODIS}) + b \cdot (((1 - \alpha_{MAR}) \cdot SW_{in,MAR}) - ((1 - \alpha_{MODIS}) \cdot SW_{in,MODIS})). \quad (2.4)$$

Then, using the simplification:

$$T_{MAR} = T_{MODIS}, \quad SW_{in,MAR} = SW_{in,MODIS}, \quad (2.5)$$

Equation 2.4 can be rewritten as:

$$\Delta R = b \cdot SW_{in} \cdot (\alpha_{MODIS} - \alpha_{MAR}). \quad (2.6)$$

The values for  $\alpha_{MODIS}$  and  $\alpha_{MAR}$  are known and the values for  $SW_{in}$  are taken directly from MAR output, which includes effects of solar zenith angle and surface slope. Then,  $b$  is determined from a linear regression analysis, shown by Figure 2.3, of absorbed shortwave radiation and runoff, as modelled by MAR. In this linear regression I omit non-melting days, i.e. days with no runoff, as the shortwave radiation factor should represent the effect on production of melt of additional absorbed shortwave radiation on melting days. A value of  $0.2335 \text{ m}^2 \text{ mm W}^{-1} \text{ day}^{-1}$  is found for the slope, which is forced to go through the origin (0,0). The value for the slope represents the shortwave radiation factor  $b$ . Although the  $R^2$ -value is merely -0.1468, the value for  $b$  found here is similar to the value found by Pellicciotti et al., 2005 of  $0.2256 \text{ m}^2 \text{ mm W}^{-1} \text{ day}^{-1}$  for the shortwave radiation factor. The value for  $b$  found from this linear regression is thus assumed to be significant.

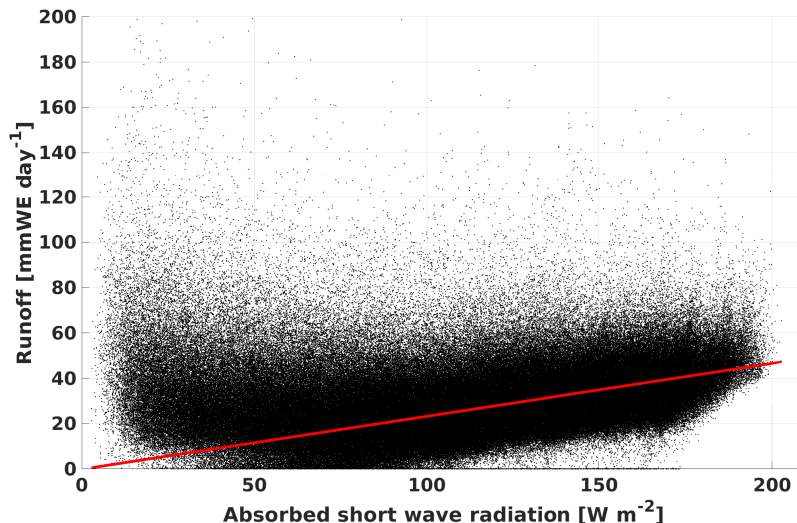


Figure 2.3: Linear regression of absorbed shortwave radiation versus runoff, as modelled by MAR. A value of  $0.2335 \text{ m}^2 \text{ mm W}^{-1} \text{ day}^{-1}$  ( $R^2=-0.1468$ ) is found for the slope, representing the shortwave radiation factor  $b$ .

## 2.4 Results and discussion

### 2.4.1 Inter-annual bare ice extent

As a first step in assessing MAR’s performance in modelling runoff from the bare ice zone, I determined how well it captures the bare ice extent and its variability as compared to MODIS. The inter-annual maximum bare ice extent in square kilometers for 2000-2018 for MAR and MODIS is shown in Figure 2.4. The orange, green, red and blue solid lines and the dashed blue line represent the results from MAR, forced with ERA5, on horizontal model resolutions of 7.5, 10, 15 and 20 km, and forced with NCEP1 on a horizontal model resolution of 20 km, respectively. The black and grey lines represent the lower and upper boundaries for MODIS, with the grey shaded area representing the uncertainty due to cloud-obstruction.

The patterns of inter-annual maximum bare ice extent from both MAR and MODIS correspond well, with high  $R^2$ -values over 0.89 for each combination of MAR and MODIS. Table 2.1 shows the correlation values of

each MAR resolution and forcing with the mean of the lower and upper boundaries of the MODIS maximum bare ice extent. All P-values are below  $10^{-9}$ , confirming significance of the correlation values.

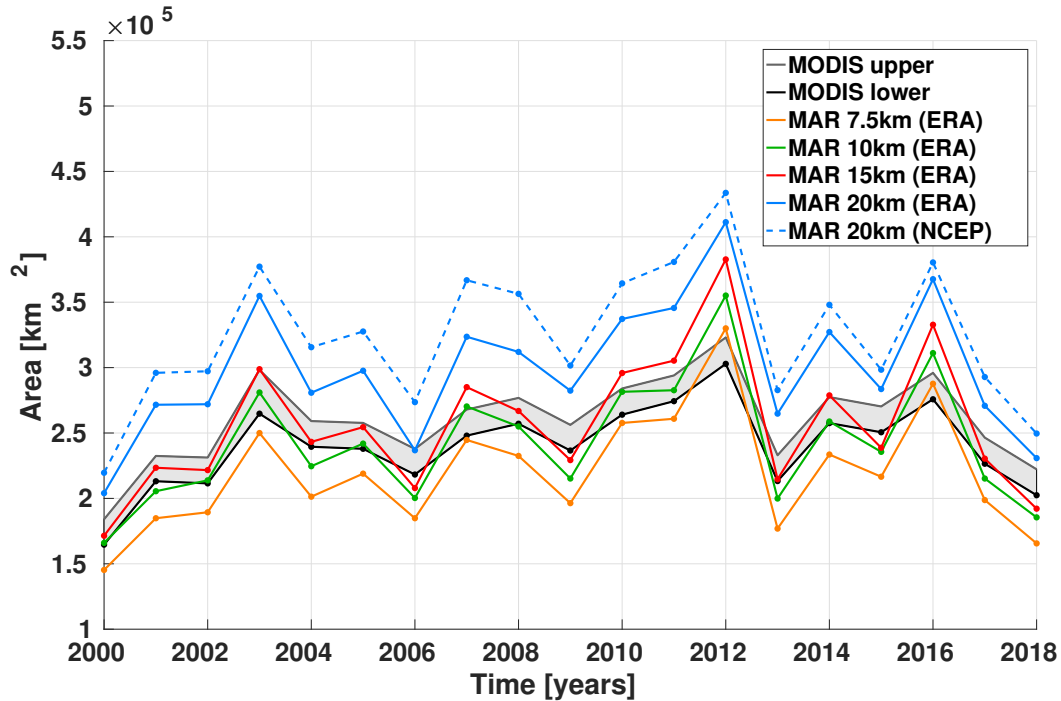


Figure 2.4: Time series of the inter-annual maximum bare ice extent for 2000-2018 for MAR and MODIS. The shaded grey area represents the cloud uncertainty of the MODIS estimate.

Correlation with MODIS	$R^2$
MAR 7.5km (ERA5)	0.905
MAR 10km (ERA5)	0.900
MAR 15km (ERA5)	0.895
MAR 20km (ERA5)	0.912
MAR 20km (NCEP1)	0.909

Table 2.1:  $R^2$ -values of the correlation of the inter-annual maximum bare ice extent for 2000-2018 for MODIS and MAR on each resolution and climate forcing.

The extreme melt years 2012 and 2016, as well as the extreme low melt year 2013 (Noël et al., 2019 and Ryan et al., 2019), are captured well by both MAR and MODIS. The results from MAR on model resolutions of 10 and 15 km correspond best with the results from MODIS in terms of the mean maximum bare ice extent over 2000-2018 (Table 2.2). Except for the extreme melt years 2012 and 2016, where MAR overestimates the maximum bare ice extent with respect to MODIS. The maximum bare ice extent for these extreme melt years are captured best by MAR on 7.5 km, while this MAR result underestimates the maximum bare ice extent with respect to MODIS during the rest of the study period. A higher model resolution would be expected to resolve more small-scale processes on the ice sheet and thus provide a more realistic estimate of the maximum bare ice extent. However, the result for MAR on the highest resolution (7.5 km) seems to have a larger bias with the MODIS result than the results for MAR on 10 and 15 km. This might be an indication that the bare ice detection algorithm for MODIS erroneously detects some pixels containing

firm as bare ice and thus overestimates the actual bare ice extent. It might also be an indication that the bare ice detection algorithm for MAR mistakenly excludes some bare ice and thus underestimates the actual modelled bare ice extent. The MAR results on 20 km, forced with both ERA5 and NCEP1, overestimate the bare ice extent with respect to MODIS during the entire study period. Here, the results for NCEP1 are significantly higher than for ERA5. This might be an artefact of the lower horizontal spatial and temporal resolution of NCEP1 ( $2.5 \times 2.5^\circ$ , 6-hourly) compared to ERA5 ( $0.28 \times 0.28^\circ$ , hourly).

	Mean [ $10^5 \text{ km}^2$ ]	Trend [ $10^3 \text{ km}^2 \text{ yr}^{-1}$ ]
MODIS 0.5km (lower)	$2.399 \pm 0.320$	1.960
MODIS 0.5km (upper)	$2.604 \pm 0.329$	1.841
MAR 7.5km (ERA5)	$2.198 \pm 0.452$	2.224
MAR 10km (ERA5)	$2.421 \pm 0.471$	2.071
MAR 15km (ERA5)	$2.565 \pm 0.512$	2.232
MAR 20km (ERA5)	$2.987 \pm 0.513$	2.053
MAR 20km (NCEP1)	$3.243 \pm 0.531$	1.496

Table 2.2: Mean and trend of the inter-annual maximum bare ice extent over 2000-2018 for MAR and MODIS.

The values for the mean and trend over 2000-2018 for MAR and MODIS are shown in Table 2.2. Among the MAR and MODIS results, trends of  $1.496 - 2.232 \cdot 10^3 \text{ km}^2 \text{ yr}^{-1}$  are found, amounting to an increase of  $0.46 - 1.01\%$  of the respective mean maximum bare ice extent per year.

#### 2.4.2 Intra-annual bare ice extent

To evaluate how well MAR models the evolution of the bare ice extent with respect to observations from MODIS, I determined the intra-annual bare ice extent during JJA, averaged over 2000-2018. Figure 2.5 shows the results for each MAR resolution and forcing and the result for MODIS, using the same color coding as the inter-annual results. In this case, the shaded grey band represents the full area that is covered by clouds per day. The MODIS cloud-uncertainty band is larger in this intra-annual result as for the inter-annual result only pixels flagged as clouds for at least 90% of the days in JJA are included in the uncertainty. This increased cloud-uncertainty makes intra-annual comparison of MAR with MODIS less robust than the inter-annual comparison.

All MAR and MODIS results show a similar pattern of increasing bare ice extent starting in early June and peak in late July to early August. The correlation between MAR and MODIS is complicated to evaluate due to the high cloud-uncertainty for MODIS. However, the MAR results on 7.5, 10 and 15 km lie almost completely within the lower and upper MODIS bounds and show very high correlation with each other. In general, a higher model resolution for MAR results in a lower bare ice extent, similar to the inter-annual results. The MAR results on 20 km show an overestimation of the bare ice extent with respect to MODIS during the peak in late July and early August. Again, using NCEP1 as climate forcing, as opposed to ERA5, results in a higher bare ice extent over the entire period.

Average summer surface temperatures over the GrIS are highest in early July, as shown in Figure 2.6 in orange, indicating that exposure of bare ice due to increased surface temperatures over the GrIS experiences a delay of several weeks. The bare ice extent from MAR shows a clear dip in late July. The lower bound for the MODIS-derived bare ice extent exhibits a similar, though slightly smaller dip. In reality, the dip for MODIS may be as apparent as for MAR. However, this pattern is not discernible due to the cloud-uncertainty

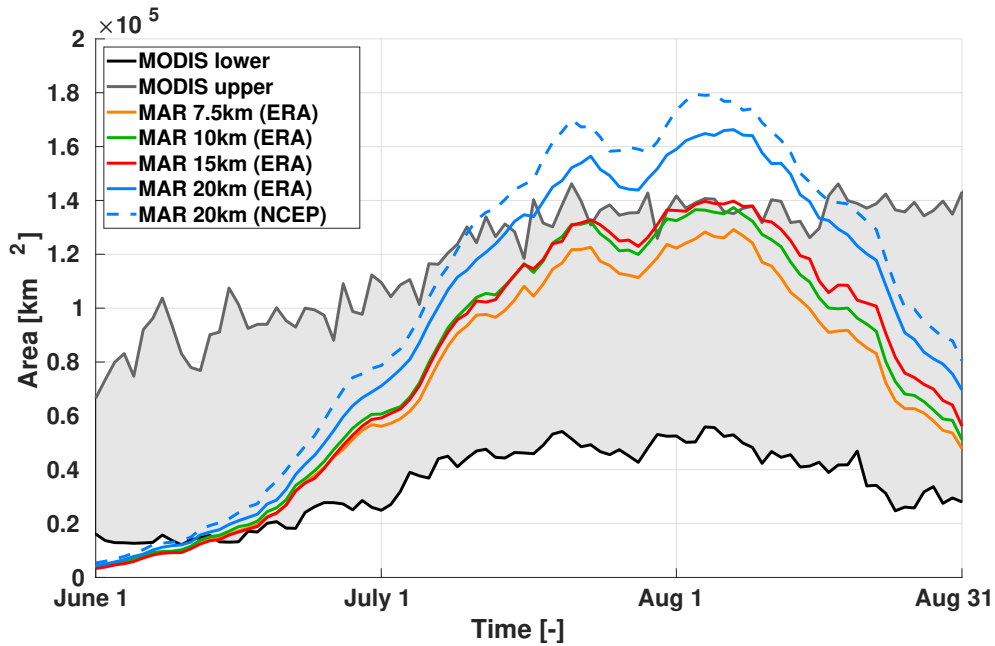


Figure 2.5: Time series of the average intra-annual maximum bare ice extent for 2000-2018 for MAR and MODIS. The shaded grey area represents the cloud uncertainty of the MODIS estimate.

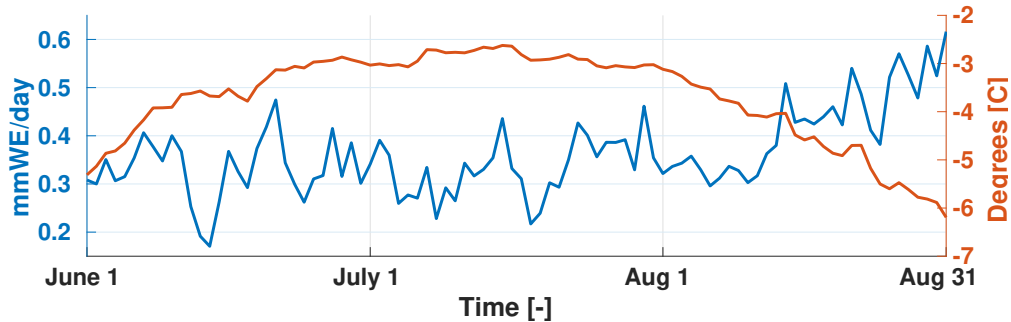


Figure 2.6: Time series of the average snowfall and surface temperature over the GrIS in JJA for 2000-2018, as modelled by MAR.

in MODIS. Figure 2.6 shows the average summer snowfall over the GrIS in blue, with a multi-day peak in late July indicating that the the dip in bare ice extent is possibly due to increased snowfall events during this period, covering bare ice and reducing bare ice extent.

### 2.4.3 Bare ice albedo

The average albedo on the overlapping bare ice extent as modelled by MAR and observed with MODIS is shown in Figure 2.7, for MAR (dashed) and MODIS (solid), averaged over 2000-2018. The results indicate that MAR overestimates bare ice albedo by 0.044-0.054 during JJA with respect to MODIS, depending on resolution and climate forcing. The results for MAR exhibit low variability during the study period, shown by the means and standard deviations in Table 2.3, as was expected from MAR's bare ice albedo scheme. Moreover, differences in the results between each MAR resolution and climate forcing are small. The results for MODIS exhibit a variability twice as high as the variability for MAR during the study period, though variability in the mean bare ice albedo for each resolution and climate forcing is small.

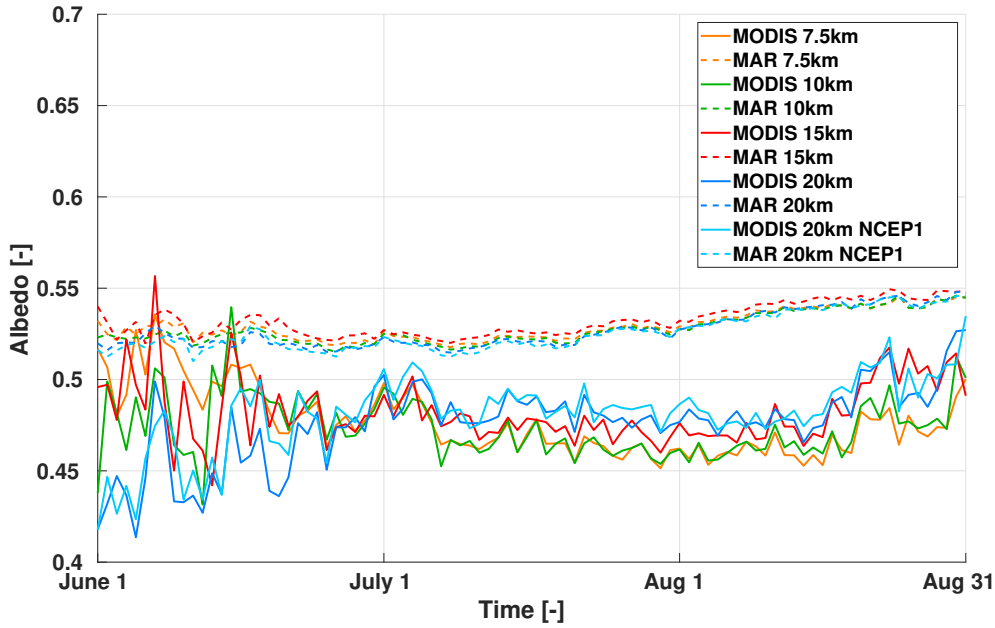


Figure 2.7: Time series of the average bare ice albedo in JJA over 2000-2018 for MAR and MODIS.

	MAR	MODIS
7.5km (ERA5)	$0.529 \pm 0.008$	$0.477 \pm 0.019$
10km (ERA5)	$0.528 \pm 0.008$	$0.473 \pm 0.017$
15km (ERA5)	$0.532 \pm 0.009$	$0.482 \pm 0.018$
20km (ERA5)	$0.527 \pm 0.010$	$0.476 \pm 0.022$
20km (NCEP1)	$0.526 \pm 0.010$	$0.481 \pm 0.021$

Table 2.3: Mean bare ice albedo during JJA in 2000-2018 for MAR and MODIS.

The MODIS results in June show an extremely high variability. This is due to the minimal bare ice extent on the GrIS in early summer and the even smaller overlapping bare ice extent in both MAR and MODIS. Hence, for some days in June only a small number of pixels are available from which to determine the average bare ice albedo. This variability is clearly seen in the average bare ice albedo maps over 2000-2018 for MODIS in Figure 2.8a as opposed to MAR in Figure 2.8b. These maps depict the full bare ice extent that is at one time simultaneously modelled by MAR and observed with MODIS during JJA in 2000-2018. Where MAR exhibits low variability over the entire GrIS, MODIS shows significant variability. This is in part due to some snowfall events over the bare ice zone which can alter the surface albedo slightly. These events are not fully captured by MAR however. MODIS shows bare ice albedo values higher than expected in the northern section of the ice sheet. This may be an artefact of the positively biased MOD10A1 product above latitudes of  $70^\circ$ . These anomalously high bare ice albedo values may also indicate that the bare ice detection algorithm for MODIS should be improved as it may erroneously detect firn, with a higher albedo, as bare ice in some cases.

Large sections of low albedo values ( $< 0.4$ ) are featured in the Southwestern region of the GrIS, which is termed the dark ice zone. These low albedo values in the dark ice zone possibly indicate the presence of abundant light-absorbing impurities, such as ice algal blooms as previously discussed by Wang et al., 2018, Cook et al., 2020 and Williamson et al., 2020. These impurities are not represented in the bare ice albedo scheme used in MAR (Tedesco et al., 2016a). The large negative albedo bias in the dark ice zone Figure

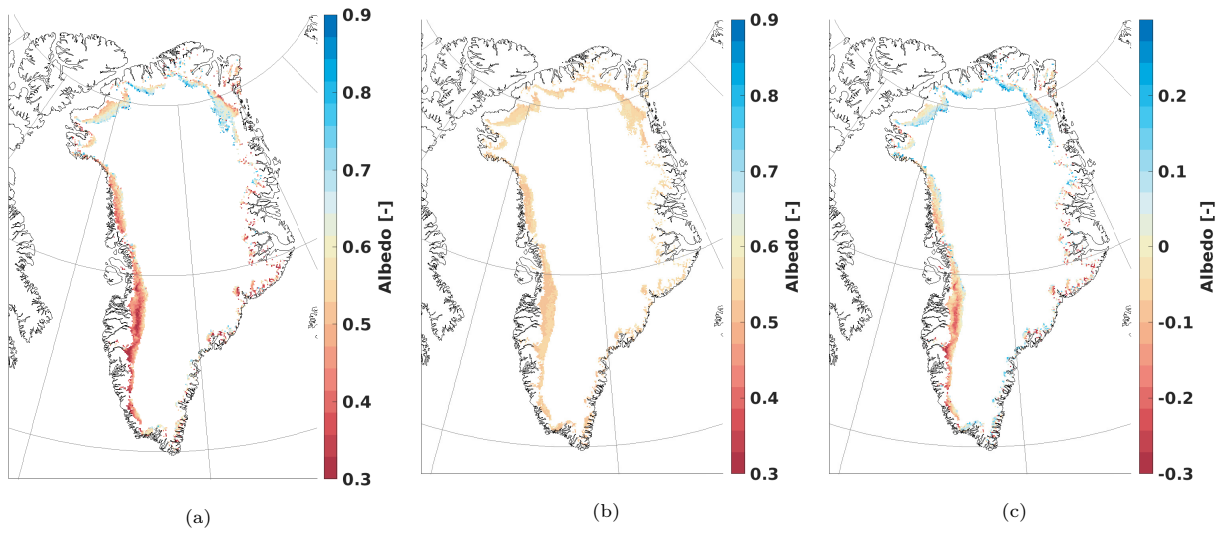


Figure 2.8: Maps of average bare ice albedo in JJA over 2000-2018 on 7.5 km resolution, for: a) MODIS, b) MAR, and c) their difference (MAR-MODIS).

(2.8c), thus indicates a significant overestimation of bare ice albedo by MAR. Conversely, a positive bias in bare ice albedo is observed along the margins of the Southeastern and Northern GrIS, with the latter possibly due to the positively biased MOD10A1 product.

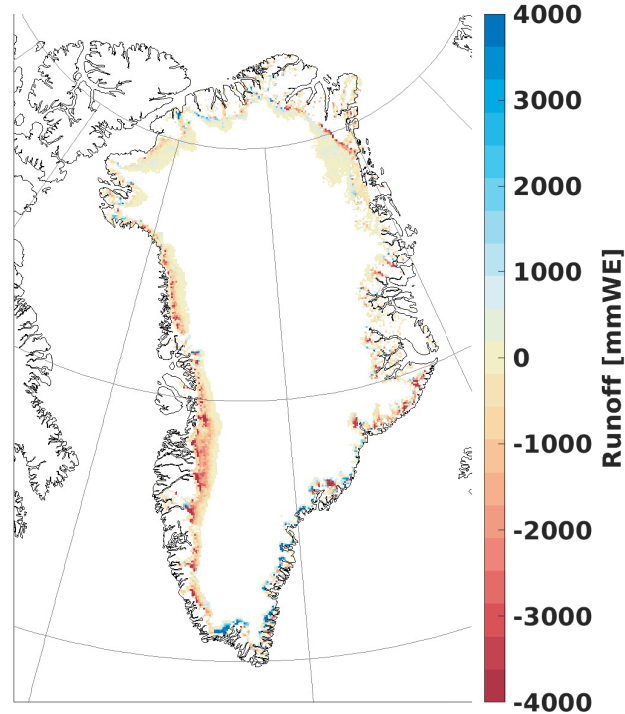


Figure 2.9: Map of the bias in total runoff over the bare ice zone on the GrIS in JJA over 2000-2018 for 7.5 km resolution when using the difference between bare ice albedo as modelled by MAR and as observed with MODIS.

#### 2.4.4 Runoff

Using the energy balance model by Pellicciotti et al., 2005, an estimate is determined for the bias in runoff as described in Equation 2.4. The empirical coefficient  $b$  from Section 2.3.4 is used and the incoming shortwave radiation is taken from MAR output. Then, using the difference in bare ice albedo, as modelled by MAR and as observed with MODIS, an underestimation in runoff of  $\sim 7 \text{ Gtonyr}^{-1}$  on average from the bare ice zone is calculated during JJA in 2000-2018. The total bias in runoff from the bare ice zone by MAR over 2000-2018 amounts to an underestimation of  $\sim 128 \text{ Gton}$ . The calculated bias in runoff is not significant when compared to the annual mass loss from the GrIS of  $254 \pm 18 \text{ Gtonyr}^{-1}$  over 2005-2015 (Shepherd et al., 2020). However, Figure 2.9 illustrates that the majority of the underestimation in runoff emanates from the dark ice zone. Contrarily, an overestimation in runoff is observed along the margins of the Southeastern region of the GrIS. The unrealistically high bare ice albedo values in the Northern section of the GrIS as observed with MODIS reduce the overall albedo bias, possibly reducing the runoff bias. It is thus possible that the underestimation of runoff from MAR should be larger and more significant. As the relation between absorbed shortwave radiation and runoff (i.e. the empirical coefficient  $b$ ) changes over the summer months, a more realistic bias in runoff may be determined when using a coefficient  $b$  determined for each week, as opposed to only one coefficient for the entire summer.

## 2.5 Conclusion

In this thesis I evaluated the performance of a regional climate model (MAR) with respect to satellite imagery (MODIS) during the summer months June, July and August during 2000-2018. I focused on assessing the performance of MAR in modelling bare ice extent and bare ice albedo on the GrIS. MAR is evaluated on horizontal model resolutions of 7.5, 10, 15 and 20 km, using ERA5 and NCEP1 as climate forcings. As a last step, I used the bias in bare ice albedo, as modelled by MAR and as observed with MODIS, to infer the accessory bias in runoff from the bare ice zone. The results presented in this thesis reveal areas of agreement as well as discrepancies between modelled and remotely sensed bare ice characteristics.

The results indicate that the inter-annual maximum bare ice extent as modelled by MAR exhibits high correlation with the results from MODIS, with  $R^2$ -values over 0.89 and  $P$ -values below  $10^{-9}$ . However, variations exist between the mean annual maximum bare ice extent over 2000-2018 as modelled by MAR and observed with MODIS, ranging from 2.2 to  $3.2 \cdot 10^5 \text{ km}^2$ , where a higher model resolution results in a lower maximum bare ice extent. The differences in the mean values for the maximum bare ice extent seem likely to be a result of inaccuracies in the bare ice detection algorithm for either or both MAR and MODIS, particularly as a high correlation is observed between model and observations. Furthermore, trends for the inter-annual maximum bare ice extent from 2000 to 2018 are found of  $1.50 - 2.23 \cdot 10^3 \text{ km}^2\text{yr}^{-1}$ , amounting to 0.46 - 1.01% of the respective mean maximum bare ice extent.

Comparison of the intra-annual bare ice extent is less straightforward as daily bare ice detections from MODIS are largely obstructed by clouds, creating a significant uncertainty in the actual remotely sensed bare ice extent. Nonetheless, high correlation is observed between each MAR model resolution and climate forcing, where again a higher model resolution results in a lower bare ice extent. The bare ice extents from both MAR and MODIS show an increasing trend starting in early June and a peak in early August. Comparison with average surface temperatures on the GrIS, peaking in early July, suggests that a delay may exist between increasing surface temperatures and exposure of bare ice. A dip in bare ice extent in late July is observed in results from both MAR and MODIS. Average snowfall over the GrIS shows a peak in the same period, indicating that the dip in bare ice extent may be a result of some snowfall events.

The results presented here show that MAR overestimates bare ice albedo by  $0.044 - 0.054$  on average during JJA in 2000-2018, depending on the model resolution and climate forcing. Low variability is observed in the bare ice albedo values as modelled by MAR, as expected from MAR's bare ice albedo scheme. However, mean bare ice albedo values during JJA in 2000-2018 are rather similar for each resolution and climate forcing, for both MAR and MODIS. Bare ice albedo values as observed with MODIS show high variability. Extremely high albedo values are found in the Northern section of the GrIS, though this might be an artefact of the positively biased MOD10A1 product. Extremely low average albedo values ( $< 0.4$ ) are found in the dark ice zone, induced by high amounts of light-absorbing impurities such as dust, cryoconite and ice algal blooms. These impurities are not modelled or parameterized by MAR, bringing forth a significant overestimation of albedo in the dark ice zone.

Lastly, an energy balance model is used to infer a bias in runoff as induced by the bare ice albedo bias. An underestimation by MAR of runoff from the bare ice zone is determined of  $\sim 7 \text{ Gtonyr}^{-1}$  on average during JJA in 2000-2018. This amounts to a total of  $\sim 128 \text{ Gton}$  over the entire period 2000-2018. This bias is not significant on the annual GrIS mass loss. However, the majority of negative runoff bias originates from the dark ice zone, while a positive runoff bias is observed along the margins of the Southeastern section of the GrIS. The unrealistically high albedo values in the Northern section of the GrIS may have resulted in a more moderate underestimation of total runoff from the GrIS. Furthermore, using a coefficient value for the relation between absorbed shortwave radiation and runoff derived weekly as opposed to one coefficient for the entire summer may result in a more realistic estimate of the runoff bias.

Future research should be directed towards understanding which sources contribute to the discrepancies between modelled and remotely sensed bare ice albedo. This includes processes of exposure, accumulation and production of light-absorbing impurities on ice, especially in the dark ice zone, as well as processes governing clouds and solar radiation. A proper bare ice albedo scheme, including these processes governing impurities, may result in a more realistic representation of bare ice albedo in climate models. Subsequently, this may result in more accurate projections of runoff from the GrIS.

# Appendices

## A Sea level equation

The processes governing RSL and GIA are for the first time collectively described by Farrell and Clark, 1976 as the sea level equation (SLE). The authors present an exact method for determining sea level changes as a result of changes in ice and ocean mass on the surface of an elastic and Maxwell viscoelastic non-rotating Earth model. A generalized SLE is described by Mitrovica and Milne, 2003, including a time-varying shoreline geometry and a rotating Earth. Later, Kendall et al., 2005 introduced Love number theory for the viscoelasticity to derive an extended pseudo-spectral numerical algorithm to effectively and iteratively solve the SLE. Dalca et al., 2013 extended on this theory by incorporating sediment redistribution into the gravitationally self-consistent SLE and Austermann and Mitrovica, 2015 further explored the extension of including solid Earth and gravity perturbations associated with mantle convection. The GIA model used in this thesis is mostly based on the theory described in Kendall et al., 2005 including a slight reformulation discussed in Dalca et al., 2013.

Sea level ( $SL$ ) is defined as the difference between the surface of the solid Earth ( $R$ ) including land-based and grounded marine-based ice thickness ( $I$ ), and the sea surface equipotential ( $G$ ), as given by:

$$SL = G - (R + I). \quad (\text{A.1})$$

The quantities in Equation A.1 are dependent on time  $t$  and position in terms of colatitude  $\theta$  and east longitude  $\phi$ , such that  $SL = SL(t_j, \theta, \phi)$ , for each time step  $j$ . For brevity, all quantities are expressed without these dependencies, only denoting the time step  $j$  as a subscript when needed.

The ocean height ( $S$ ) is defined as the sea level in those locations on Earth defined as ocean:

$$S = SL \cdot C, \quad (\text{A.2})$$

with  $C$  defining those locations by  $C = 1$  if  $SL > 0$  and  $C = 0$  if  $SL \leq 0$ . Topography ( $T$ ) is defined as the opposite of sea level:

$$T = -SL = -G + (R + I) \quad (\text{A.3})$$

and the total mass load ( $L$ ) on the surface, constituted of ocean water with density  $\rho_w$  and ice with density  $\rho_I$  is defined as:

$$L = S \cdot \rho_w + I \cdot \rho_I. \quad (\text{A.4})$$

The purpose of the sea level equation is to determine the elevation perturbation from some initial state of the bedrock and sea surface through changes in water and ice. All of the above mentioned quantities can be expressed in terms of their initial value at time  $t_0$  plus a perturbation at some time  $t_j$ , such as:

$$SL_j = SL_0 + \Delta SL_j. \quad (\text{A.5})$$

Using this notation, sea level change can be written as:

$$\Delta SL_j = SL_j - SL_0 = \Delta G_j - (\Delta R_j + \Delta I_j). \quad (\text{A.6})$$

As the function  $C$  is time-dependent, translation of Equation A.6 into ocean height change requires an adapted relationship that takes into account shoreline migration and initial topography  $T_0$  as follows:

$$\Delta S_j = \Delta SL_j \cdot C_j - T_0 \cdot \Delta C_j. \quad (\text{A.7})$$

Since the ocean height  $\Delta S_j$  is dependent on perturbations in  $R$  and  $G$  due to changes in surface mass loading and both  $\Delta R_j$  and  $\Delta G_j$  are in turn dependent on ocean height. This highlights the integral structure of the SLE.

The decomposition of the sea surface equipotential perturbation into globally uniform and location-dependent terms is common practice in sea level theory (Farrell and Clark, 1976). Equation ?? can in this sense be rewritten as:

$$\Delta G_j = \frac{\Delta \Phi_j}{g} + \Delta G_{loc,j}^{load}, \quad (\text{A.8})$$

with  $G_{loc}$  representing the location-dependent component of  $G$ . Dividing the variable  $\Delta \Phi_j$  by the gravitational acceleration on the surface ( $g$ ) denotes the globally uniform perturbation in the height of the sea surface equipotential. This variable takes into account changes in the ocean basin shape through deformation due to mass loading, as well as changes in ocean mass due to global ice mass variations.

Then, Equation A.6 can be rewritten as:

$$\Delta S L_j = \frac{\Delta \Phi_j}{g} + \Delta G_{loc,j}^{load} - (\Delta R_j^{load} + \Delta I_j). \quad (\text{A.9})$$

Or, in terms of globally uniform and location-dependent terms:

$$\Delta S L_j = \frac{\Delta \Phi_j}{g} + \Delta S L_{loc,j}, \quad (\text{A.10})$$

with

$$\Delta S L_{loc,j} = \Delta G_{loc,j}^{load} - (\Delta R_j^{load} + \Delta I_j). \quad (\text{A.11})$$

The SLE can then be written as:

$$\Delta S_j = \left( \frac{\Delta \Phi_j}{g} \right) C_j + \Delta S L_{loc,j} \cdot C_j - T_0 \cdot \Delta C_j. \quad (\text{A.12})$$

The globally uniform term for sea surface equipotential perturbations  $\Delta \Phi_j/g$  can be solved by integrating Equation A.12:

$$\frac{\Delta \Phi_j}{g} = -\frac{1}{\mathcal{M}_j} \left[ \frac{\rho_I}{\rho_w} \iint_{\mathcal{A}} \Delta I_j d\mathcal{A} + \iint_{\mathcal{A}} \Delta S L_{loc,j} \cdot C_j d\mathcal{A} - \iint_{\mathcal{A}} T_0 \cdot \Delta C_j d\mathcal{A} \right]. \quad (\text{A.13})$$

And requiring conservation of mass of the combined ocean and ice volumes over Earth's surface  $\mathcal{A}$ :

$$0 = \rho_I \iint_{\mathcal{A}} \Delta I_j d\mathcal{A} + \rho_w \iint_{\mathcal{A}} \Delta S_j d\mathcal{A}, \quad (\text{A.14})$$

with

$$\mathcal{M}_j = \iint_{\mathcal{A}} C_j d\mathcal{A}. \quad (\text{A.15})$$

Solving the SLE (Equation A.12) requires integration, as there exists a co-dependency of terms on either side of the equation. In computational terms, this calls for iteratively solving the SLE. Here, at each time step  $j$  a first guess for  $\Delta S_j$  is used for computing the right-hand-side of the equation.  $\Delta S L_{loc,j}$  is solved using Love numbers which are calculated using the mass load as in Equation A.4. The solution of the right side of the equation equals a revised estimate of  $\Delta S_j$ , which is then again used as input for the right-hand-side

of the equation. This process is repeated until convergence is reached after which the next time step is solved.

A first guess of  $\Delta S_j$  is commonly a uniform distribution of the added (or removed) water without deformation of the bedrock. A check is included when solving the SLE ensuring sufficient ice thickness ( $I_j$  and  $\Delta I_j$ ) in marine sectors for the ice to be grounded. If this check is not met, i.e. if the ice is floating, this ice is removed. A requirement for solving the SLE is that the initial topography  $T_0$  is known. A first guess for  $T_0$  is used to start the initial iteration with which sea level changes are computed over the entire time range of the model. Then,  $T_0$  is updated from the difference between the observed and computed present-day topography and the entire iteration is repeated until the difference between observed and computed present-day topography is below a specified value.

## References

- Alexander, P.M., Tedesco, M., Fettweis, X., Wal, R.S.W. van de, Smeets, C.J.P.P., and Broeke, M.R. van den (2014). “Assessing spatio-temporal variability and trends in modelled and measured Greenland Ice Sheet albedo (2000–2013)”. *The Cryosphere* 8, pp. 2293–2312. DOI: 10.5194/tc-8-2293-2014.
- Argus, D.F., Peltier, W.R., Drummond, R., and Moore, A.W. (2014). “The Antarctica component of post-glacial rebound model ICE-6G\_C (VM5a) based on GPS positioning, exposure age dating of ice thicknesses, and relative sea level histories”. *Geophysical Journal International* 198.1, pp. 537–563. DOI: 10.1093/gji/ggu140.
- Austermann, J. and Mitrovica, J.X. (2015). “Calculating gravitationally self-consistent sea level changes driven by dynamic topography”. *Geophysical Journal International* 203.3, pp. 1909–1922. DOI: 10.1093/gji/ggv371.
- Austermann, J., Mitrovica, J.X., Latychev, K., and Milne, G.A. (2013). “Barbados-based estimate of ice volume at Last Glacial Maximum affected by subducted plate”. *Nature Geoscience* 6.7, pp. 553–557. DOI: 10.1038/ngeo1859.
- Bamber, J.L., Ekholm, S., and Krabill, W.B. (2001). “A new, high-resolution digital elevation model of Greenland fully validated with airborne laser altimeter data”. *Journal of Geophysical Research* 106, pp. 6733–6745.
- Bamber, J.L., Westaway, R.M., Marzeion, B., and Wouters, B. (2018). “The land ice contribution to sea level during the satellite era”. *Environmental Research Letters* 13. DOI: 10.1088/1748-9326/aac2f0.
- Box, J.E. (2013). “Greenland Ice Sheet Mass Balance Reconstruction. Part II: Surface Mass Balance (1840–2010)”. *Journal of Climate* 26, pp. 6974–6989. DOI: 10.1175/JCLI-D-12-00518.1.
- Box, J.E., Fettweis, X., Stroeve, J.C., Tedesco, M., Hall, D.K., and Steffen, K. (2012). “Greenland ice sheet albedo feedback: thermodynamics and atmospheric drivers”. *The Cryosphere* 6, pp. 821–839. DOI: 10.5194/tc-6-821-2012.
- Briner, J.P., Stewart, H.A.M., Young, N.E., Philipps, W., and Losee, S. (2010). “Using proglacial-threshold lakes to constrain fluctuations of the Jakobshavn Isbræ ice margin, western Greenland, during the Holocene”. *Quaternary Science Reviews* 29.27-28, pp. 3861–3874. DOI: 10.1016/j.quascirev.2010.09.005.
- Broeke, M. Van Den, Bamber, J., Ettema, J., Rignot, E., Schrama, E., Berg, W. J. Van De, Meijgaard, E. Van, Velicogna, I., and Wouters, B. (2009). “Partitioning Recent Greenland Mass Loss”. *Science* 326.5955, pp. 984–986. DOI: 10.1126/science.1178176.
- Broeke, M. van den, Box, J., Fettweis, X., Hanna, E., Noël, B., Tedesco, M., As, D. van, Berg, W.J. van de, and Kampenhout, L. van (2017). “Greenland Ice Sheet Surface Mass Loss: Recent Developments in Observation and Modeling”. *Current Climate Change Reports* 3, pp. 345–356. DOI: 10.1007/s40641-017-0084-8.

- Broeke, M. van den, Enderlin, E.M., Howat, I.M., Kuipers Munneke, P., Noël, B., Berg, W.J. van de, Meijgaard, E. van, and Wouters, B. (2016). “On the recent contribution of the Greenland ice sheet to sea level change”. *The Cryosphere* 10, pp. 1933–1946. DOI: 10.5194/tc-10-1933-2016.
- Chen, X., Zhang, X., Church, J.A., Watson, C.S., King, M.A., Monselesan, D., Legresy, B., and Harig, C. (2017). “The increasing rate of global mean sea-level rise during 1993–2014”. *Nature Climate Change* 7, pp. 492–497. DOI: 10.1038/NCLIMATE3325.
- Church, J.A., Clark, P.U., Cazenave, A., Gregory, J.M., Jevrejeva, S., Levermann, A., Merrifield, M.A., Milne, G.A., Nerem, R.S., Nunn, P.D., Payne, A.J., Pfeffer, W.T., Stammer, D., and Unnikrishnan, A.S. (2013). “Sea Level Change”. *Climate Change 2013: The Physical Science Basis. Contribution of Working Group I to the Fifth Assessment Report of the Intergovernmental Panel on Climate Change*. Ed. by T.F. Stocker, D. Qin, G.-K. Plattner, M. Tignor, S.K. Allen, J. Boschung, A. Nauels, Y. Xia, V. Bex, and P.M. Midgley. Cambridge, United Kingdom and New York, NY, USA: Cambridge University Press. Chap. 13, pp. 1137–1216. DOI: 10.1017/CB09781107415324.026.
- Clark, P.U., Dyke, A.S., Shakun, J.D., Carlson, A.E., Clark, J.A., Wohlfarth, B., Mitrovica, J.X., Hostetler, S.W., and McCabe, A.M. (2009). “The Last Glacial Maximum”. *Science* 325, pp. 710–714. DOI: 10.1126/science.1172873.
- Connolly, James A.D. (2005). “Computation of phase equilibria by linear programming: A tool for geodynamic modeling and its application to subduction zone decarbonation”. *Earth and Planetary Science Letters* 236, pp. 524–541.
- Cook, J.M., Edwards, A., Mur, L.A.J., Cook, S., Gokul, J.K., Cameron, K.A., Sweet, M., and Irvine-Fynn, T.D.L. (2016). “Metabolome-mediated biocryomorphic evolution promotes carbon fixation in Greenlandic cryoconite holes”. *Environmental Microbiology* 18.12, pp. 4674–4686. DOI: 10.1111/1462-2920.13349.
- Cook, J.M., Tedstone, A.J., Williamson, C., McCutcheon, J., Hodson, A.J., Dayal, A., Skiles, M., Hofer, S., Bryant, R., McAree, O., McGonigle, A., Ryan, J., Anesio, A.M., Irvine-Fynn, T.D.L., Hubbard, A., Hanna, E., Flanner, M., Mayanna, S., Benning, L.G., As, D. van, Yallop, M., McQuaid, J.B., Gribbin, T., and Tranter, M. (2020). “Glacier algae accelerate melt rates on the south-western Greenland Ice Sheet”. *The Cryosphere* 14.1, pp. 309–330. DOI: 10.5194/tc-14-309-2020.
- Dahl-Jensen, D., Mosegaard, K., Gundestrup, N., Clow, G.D., Johnsen, S.J., Hansen, A.W., and Balling, N. (1998). “Past Temperatures Directly from the Greenland Ice Sheet”. *Science* 282.5387, pp. 268–271. DOI: 10.1126/science.282.5387.268.
- Dalca, A.V., Ferrier, K.L., Mitrovica, J.X., Perron, J.T., Milne, G.A., and Creveling, J.R. (2013). “On post-glacial sea level - III. Incorporating sediment redistribution”. *Geophysical Journal International* 154. DOI: 10.1093/gji/ggt089.
- DeGrandpre, K.G. and Freymueller, J.T. (2019a). “Modeling sea level changes and geodetic variations by glacial isostasy: the improved SELEN code”. *Journal of Geophysical Research: Solid Earth* 124, pp. 9148–9163. DOI: 10.1029/2018JB017163.

- DeGrandpre, K.G. and Freymueller, J.T. (2019b). “Vertical Velocities, Glacial Isostatic Adjustment, and Earth Structure of Northern and Western Alaska Based on Repeat GPS Measurements”. *Journal of Geophysical Research: Solid Earth* 124, pp. 9148–9163. DOI: 10.1029/2018JB017163.
- Desbruyères, D., McDonagh, E.L., King, B.A., and Thierry, V. (2017). “Global and Full-Depth Ocean Temperature Trends during the Early Twenty-First Century from Argo and Repeat Hydrography”. *Journal of Climate* 30.6, pp. 1985–1997. DOI: 10.1175/JCLI-D-16-0396.1.
- Dziewonski, A.M. and Anderson, D.L. (1981). “Preliminary reference Earth model”. *Physics of the Earth and Planetary Interiors* 25, pp. 297–356. DOI: 10.17611/DP/9991844.
- Erofeeva, S., Padman, L., and Howard, S.L. (2020). *Tide Model Driver (TMD) version 2.5, Toolbox for Matlab*. URL: [https://www.github.com/EarthAndSpaceResearch/TMD\\_Matlab\\_Toolbox\\_v2.5](https://www.github.com/EarthAndSpaceResearch/TMD_Matlab_Toolbox_v2.5) (visited on 03/01/2020).
- Farrell, W.E. and Clark, J.A. (1976). “On Postglacial Sea Level”. *Geophysical Journal International* 46, pp. 647–667. DOI: 10.1111/j.1365-246X.1976.tb01252.x.
- Ferrier, Ken L., Austermann, Jacqueline, Mitrovica, Jerry X., and Pico, Tamara (2017). “Incorporating sediment compaction into a gravitationally self-consistent model for ice age sea-level change”. *Geophysical Journal International* 211.1, pp. 663–672. DOI: 10.1093/gji/ggx293.
- Fettweis, X., Box, J.E., Agosta, C., Amory, C., Kittel, C., Lang, C., As, D. van, Machguth, H., and Gallee, H. (2017). “Reconstructions of the 1900–2015 Greenland ice sheet surface mass balance using the regional climate MAR model”. *The Cryosphere* 11, pp. 1015–1033. DOI: 10.5194/tc-11-1015-2017.
- Fettweis, X., Hanna, E., Lang, C., Belleflamme, A., Ericum, M., and Gallee, H. (2013). “Important role of the mid-tropospheric atmospheric circulation in the recent surface melt increase over the Greenland ice sheet”. *The Cryosphere* 7, pp. 241–248. DOI: 10.5194/tc-7-241-2013.
- Fischer, H., Meissner, K.J., and Mix A.C., et al. (2018). “Palaeoclimate constraints on the impact of 2 C anthropogenic warming and beyond”. *Nature Geoscience* 11, pp. 474–485. DOI: <https://doi.org/10.1038/s41561-018-0146-0>.
- Fleming, K. and Lambeck, K. (2004). “Constraints on the Greenland Ice Sheet since the Last Glacial Maximum from sea-level observations and glacial-rebound models”. *Quaternary Science Reviews* 23.9-10, pp. 1053–1077. DOI: 10.1016/j.quascirev.2003.11.001.
- Forman, S., Marín, L., Veen, C. Van Der, Tremper, C., and Csatho, B. (2007). “Little Ice Age and neoglacial landforms at the Inland Ice margin, Isunguata Sermia, Kangerlussuaq, west Greenland”. *Boreas* 36.4, pp. 341–351. DOI: 10.1080/00173130601173301.
- Fredskild, B. (1983). “The Holocene vegetational development of the Godthabsfjord area, West Greenland. Meddelelser Om Gromland”. *Geoscience* 10.28.
- French, S.W. and Romanowicz, B.A. (2014). “Whole-mantle radially anisotropic shear velocity structure from spectral-element waveform tomography”. *Geophysical Journal International* 199.3, pp. 1303–1327.

- Gardner, A.S. and Sharp, M.J. (2010). “A review of snow and ice albedo and the development of a newphysically based broadband albedo parameterization”. *Journal of Geophysical Research* 115. DOI: 10.1029/2009JF001444.
- Group, WCRP Global Sea Level Budget (2018). “Global sea-level budget 1993–present”. *Earth System Science Data* 10.3, pp. 1551–1590. DOI: 10.5194/essd-10-1551-2018.
- Gutenberg, B. (1941). “Changes in sea level, postglacial uplift, and mobility of the earths interior”. *Geological Society of America Bulletin* 52.5, pp. 721–772. DOI: 10.1130/gsab-52-721.
- Hall, D.K. and Riggs, G.A. (2016). *MODIS/Terra Snow Cover Daily L3 Global 500m SIN Grid, Version 6. Boulder, Colorado USA. NASA National Snow and Ice Data Center Distributed Active Archive Center.* DOI: doi.org/10.5067/MODIS/MOD10A1.006..
- Hanna, E., Cropper, T.E., Jones, P.D., Scaife, A.A., and Allan, R. (2015). “Recent seasonal asymmetric changes in the NAO (a marked summer decline and increased winter variability) and associated changes in the AO and Greenland Blocking Index”. *International Journal of Climatology* 35, pp. 2540–2554. DOI: 10.1002/joc.4157.
- Hanna, E., Fettweis, X., and Hall, R.J. (2018). “Recent changes in summer Greenland blocking captured by none of the CMIP5 models”. *The Cryosphere* 12, pp. 3287–3292. DOI: 10.5194/tc-12-3287-2018.
- Hanna, E., Fettweis, X., Mernild, S.H., Cappelen, J., Ribergaard, M.H., Shuman, C.A., Steffen, K., Wood, L., and Mote, T.L. (2014). “Atmospheric and oceanic climate forcing of the exceptional Greenland ice sheet surface melt in summer 2012”. *International Journal of Climatology* 34, pp. 1022–1037. DOI: 10.1002/joc.3743.
- Hanna, E., Mernild, S.H., Cappelen, J., and Steffen, K. (2012). “Recent warming in Greenland in a long-term instrumental (1881–2012) climatic context: I. Evaluation of surface air temperature records”. *Environmental Research Letters* 7. DOI: 10.1088/1748-9326/7/4/045404.
- Hartmann, R., Ebbing, J., and Conrad, C.P. (2020). “A Multiple 1D Earth Approach (MIDEA) to account for lateral viscosity variations in solutions of the sea level equation: An application for glacial isostatic adjustment by Antarctic deglaciation”. *Journal of Geodynamics* 135. DOI: 10.1016/j.jog.2020.101695.
- Hay, C., Mitrovica, J.X., Gomez, N., Creveling, J.R., Austermann, J., and Kopp, R.E. (2014). “The sea-level fingerprints of ice-sheet collapse during interglacial periods”. *Quaternary Science Reviews* 87, pp. 60–69. DOI: 10.1016/j.quascirev.2013.12.022.
- Hersbach, H., Bell, B., Berrisford, P., Hirahara, S., and Horanyi A., et al. (2020). “The ERA5 global reanalysis”. *Quarterly Journal of The Royal Meteorological Society*, pp. 1–51. DOI: 10.1002/qj.3803.
- Huybrechts, P. (2002). “Sea-level changes at the LGM from ice-dynamic reconstructions of the Greenland and Antarctic ice sheets during the glacial cycles”. *Quaternary Science Reviews* 21, pp. 203–231. DOI: 10013/epic.15082.d001.
- Huybrechts, P. and Wolde, J. de (1999). “The Dynamic Response of the Greenland and Antarctic Ice Sheets to Multiple-Century Climatic Warming”. *Journal of Climate* 12, pp. 2169–2188. DOI: 10.1175/1520-0442(1999)012<2169:TDR0TG>2.0.CO;2.

- IPCC (2007). “Climate Change 2007: Synthesis Report. Contribution of Working Groups I, II and III to the Fourth Assessment Report of the Intergovernmental Panel on Climate Change [Core Writing Team, Pachauri, R.K and Reisinger, A. (eds.)]. IPCC, Geneva, Switzerland”.
- Jakobs, C.L., Reijmer, C.H., Kuipers Munneke, P., Konig-Langlo, G., and Broeke, M.R. van den (2019). “Quantifying the snowmelt–albedo feedback at Neumayer Station, East Antarctica”. *The Cryosphere* 13, pp. 1473–1485. DOI: 10.5194/tc-13-1473-2019.
- Kalnay, E., Kanamitsu, M., Kistler, R., Collins, W., Deaven, D., Gandin, L., Iredell, M., Saha, S., White, G., Woollen, J., Zhu, Y., Chelliah, M., Ebisuzaki, W., Higgins, W., Janowiak, J., Mo, K.C., Ropelewski, C., Wang, J., Leetmaa, A., Reynolds, R., Jenne, R., and Joseph, D. (1996). “The NCEP/NCAR 40-Year Reanalysis Project”. *Bulletin of the American Meteorological Society* 77.3, pp. 437–472. DOI: 10.1175/1520-0477(1996)077<0437:TNYRP>2.0.CO;2.
- Kaufman, D., Ager, T., Anderson, N., Anderson, P., Andrews, J., Bartlein, P., Brubaker, L., Coats, L., Cwynar, L., Duvali, M., Dyke, A., Edwards, M., Eisner, W., Gajewski, K., Geirsdottir, A., Hu, F., Jennings, A., Kaplan, M., Kerwin, M., Lozhkin, A., MacDonald, G., Miller, G., Mock, C., Oswald, W., Otto-Bliesner, B., Porinchu, D., Ruhland, K., Smol, J., Steig, E., and Wolfe, B. (2004). “Holocene thermal maximum in the western Arctic (0–180W)”. *Quaternary Science Reviews* 23.5-6, pp. 529–560. DOI: 10.1016/j.quascirev.2003.09.007.
- Kendall, R.A., Mitrovica, J.X., and Milne, G.A. (2005). “On post-glacial sea level - II. Numerical formulation and comparative results on spherically symmetric models”. *Geophysical Journal International* 161.3, pp. 679–706. DOI: 10.1111/j.1365-246x.2005.02553.x.
- Khan, S., Sasgen, I., Bevis, M., Dam, T. van, Bamber, J., Wahr, J., Willis, M., Kjaer, K., Wouters, B., Helm, V., Castho, B., Fleming, K., Bjork, A., Aschwanden, A., Knudsen, P., and Kuipers Munneke, P. (2016). “Geodetic measurements reveal similarities between post–Last Glacial Maximum and present-day mass loss from the Greenland ice sheet”. *Science Advances* 2.9. DOI: DOI:10.1126/sciadv.1600931.
- Kjeldsen, K.K., Korsgaard, N.J., Bjørk, A.A., Khan, S.A., Box, J.E., Funder, S., Larsen, N.K., Bamber, J.L., Colgan, W., Broeke, M. van den, Siggaard-Andersen, M., Nuth, C., Schomacker, A., Andresen, C.S., Willerslev, E., and Kjær, K.H. (2015). “Spatial and temporal distribution of mass loss from the Greenland Ice Sheet since AD 1900”. *Nature* 528.7582, pp. 396–400. DOI: 10.1038/nature16183.
- Kopp, R.E., DeConto, R.M., Bader, D.A., Hay, C.C., Horton, R.M., Kulp, S., Oppenheimer, M., Pollard, D., and Strauss, B.H. (2017). “Evolving Understanding of Antarctic Ice-Sheet Physics and Ambiguity in Probabilistic Sea-Level Projections”. *Earth’s Future* 5, pp. 1217–1233. DOI: <https://doi.org/10.1002/2017EF000663>.
- Lambeck, K., Johnston, P., and Nakada, M. (1990). “Holocene glacial rebound and sea-level change in NW Europe”. *Geophysical Journal International* 103.2, pp. 451–468. DOI: 10.1111/j.1365-246x.1990.tb01784.x.
- Lecavalier, B.S., Milne, G.A., Simpson, M.J.R., Wake, L., Huybrechts, P., Tarasov, L., Kjeldsen, K.K., Funder, S., Long, A.J., Woodroffe, S., Dyke, A.S., and Larsen, N.K. (2014). “A model of Greenland ice sheet deglaciation constrained by observations of relative sea level and ice extent”. *Quaternary Science Reviews* 102, pp. 54–84. DOI: 10.1016/j.quascirev.2014.07.018.

- MacDonell, S. and Fitzsimons, S. (2008). “The formation and hydrological significance of cryoconite holes”. *Progress in Physical Geography* 32.6, pp. 595–610. DOI: 10.1177/0309133308101382.
- McLeod, J.T. and Mote, T.L. (2015). “Linking interannual variability in extreme Greenland blocking episodes to the recent increase in summer melting across the Greenland ice sheet”. *International Journal of Climatology* 36, pp. 1484–1499. DOI: 10.1002/joc.4440.
- Milne, G.A. and Mitrovica, J.X. (1998). “Postglacial sea-level change on a rotating Earth”. *Geophysical Journal International* 133, pp. 1–19. DOI: 10.1007/s00024-004-0503-3.
- Milne, G.A., Latychev, K., Schaeffer, A., Crowley, J.W., Lecavalier, B.S., and Audette, A. (2018). “The influence of lateral Earth structure on glacial isostatic adjustment in Greenland”. *Geophysical Journal International* 214.2, pp. 1252–1266. DOI: 10.1093/gji/ggy189.
- Mitrovica, J.X. and Milne, G.A. (2003). “On post-glacial sea level: I. General theory”. *Geophysical Journal International* 154, pp. 253–267. DOI: 10.1046/j.1365-246X.2003.01942.x.
- Mouginot, J., Rignot, E., Bjork, A.A., Broeke, M. van den, Millan, R., Morlighem, M., Noël, B., Scheuchl, B., and Wood, M. (2019). “Forty-six years of Greenland Ice Sheet mass balance from 1972 to 2018”. *Proceedings of the National Academy of Sciences of the United States of America* 116.19, pp. 9239–9244. DOI: 10.1073/pnas.1904242116.
- Navari, M., Margulis, S.A., Tedesco, M., Fettweis, X., and Alexander, P.M. (2018). “Improving Greenland Surface Mass Balance Estimates Through the Assimilation of MODIS Albedo: A Case Study Along the K-Transect”. *Geophysical Research Letters* 45, pp. 6549–6556. DOI: 10.1029/2018GL078448.
- Noël, B., Berg, W.J. Van De, Lhermitte, S., and Broeke, M.R. Van Den (2019). “Rapid ablation zone expansion amplifies north Greenland mass loss”. *Science Advances* 5.9. DOI: 10.1126/sciadv.aaw0123.
- Oppenheimer, M., Glavovic, B.C., Hinkel, J., Wal, R. van de, Magnan, A.K., Abd-Elgawad, A., Cai, R., CifuentesJara, M., DeConto, R.M., Ghosh, T., Hay, J., Isla, F., Marzeion, B., Meyssignac, B., and Sebesvari, Z. (2019). “Sea Level Rise and Implications for Low-Lying Islands, Coasts and Communities. In: IPCC Special Report on the Ocean and Cryosphere in a Changing Climate [H.-O. Pörtner, D.C. Roberts, V. Masson-Delmotte, P. Zhai, M. Tignor, E. Poloczanska, K. Mintenbeck, A. Alegría, M. Nicolai, A. Okem, J. Petzold, B. Rama, N.M. Weyer (eds.)]” in press.
- Pellicciotti, F., Brock, B., Strasser, U., Burlando, P., Funk, M., and Corripio, J. (2005). “An enhanced temperature-index glacier melt model including the shortwave radiation balance: development and testing for Haut Glacier d’Arolla, Switzerland”. *Journal of Glaciology* 51.175, pp. 573–587.
- Peltier, W.R. (2004). “Global glacial isostasy and the surface of the ice-age Earth: The ICE5-G (VM2) model and GRACE”. *Annual Review of Earth and Planetary Sciences* 32, pp. 111–149. DOI: 10.1146/annurev.earth.32.082503.144359.
- Peltier, W.R. and Andrews, J.T. (1976). “Glacial-Isostatic Adjustment-I. The Forward Problem”. *Geophysical Journal of the Royal Astronomical Society* 46.3, pp. 605–646. DOI: 10.1111/j.1365-246x.1976.tb01251.x.

- Peltier, W.R., Argus, D.F., and Drummond, R. (2015). “Space geodesy constrains ice age terminal deglaciation: The global ICE-6G\_C (VM5a) model: Global Glacial Isostatic Adjustment”. *Journal of Geophysical Research: Solid Earth* 120.1, pp. 450–487. DOI: 10.1002/2014JB011176.
- Peltier, W.R. and Drummond, R. (2008). “Rheological stratification of the lithosphere: A direct inference based upon the geodetically observed pattern of the glacial isostatic adjustment of the North American continent”. *Geophysical Research Letters* 35. DOI: 10.1029/2008GL034586.
- Purkey, S.G. and Johnson, G.C. (2010). “Warming of Global Abyssal and Deep Southern Ocean Waters between the 1990s and 2000s: Contributions to Global Heat and Sea Level Rise Budgets\*”. *Journal of Climate* 23.23, pp. 6336–6351. DOI: 10.1175/2010JCLI3682.1.
- Richards, F.D., Hoggard, M.J., White, N.J., and Ghelichkhan, S. (2020). “Quantifying the relationship between short-wavelength dynamic topography and thermomechanical structure of the upper mantle using calibrated parameterization of anelasticity”. *Journal of Geophysical Research: Solid Earth*. (in press). DOI: 10.1029/2019JB019062.
- Rignot, E., Velicogna, I., Broeke, M. van den, Monaghan, A., and Lenaerts, J.T.M. (2011). “Acceleration of the contribution of the Greenland and Antarctic ice sheets to sea level rise”. *Geophysical Research Letters* 38. DOI: 10.1029/2011GL046583.
- Ryan, J.C., Smith, L.C., As, D. Van, Cooley, S.W., Cooper, M.G., Pitcher, L.H., and Hubbard, A. (2019). “Greenland Ice Sheet surface melt amplified by snowline migration and bare ice exposure”. *Science Advances* 5.3. DOI: 10.1126/sciadv.aav3738.
- Schaeffer, A.J. and Lebedev, S. (2013). “Global shear speed structure of the upper mantle and transition zone”. *Geophysical Journal International* 194, pp. 417–449.
- Schaeffer, A.J. and Lebedev, S. (2014). “Imaging the North American continent using waveform inversion of global and USArray data”. *Earth and Planetary Science Letters* 402, pp. 26–41.
- Shepherd, A., Ivins, E., and Rignot, E. et al. (2020). “Mass balance of the Greenland Ice Sheet from 1992 to 2018”. *Nature* 579, pp. 233–239. DOI: 10.1038/s41586-019-1855-2.
- Simpson, M.J.R., Milne, G.A., Huybrechts, P., and Long, A.J. (2009). “Calibrating a glaciological model of the Greenland ice sheet from the Last Glacial Maximum to present-day using field observations of relative sea level and ice extent”. *Quaternary Science Reviews* 28.17-18, pp. 1631–1657. DOI: 10.1016/j.quascirev.2009.03.004.
- Slangen, A. (2012). “Modelling regional sea-level changes in recent past and future”. PhD thesis.
- Spada, G. and Galassi, G. (2012). “New estimates of secular sea level rise from tide gauge data and GIA modelling: *Secular sea level rise*”. *Geophysical Journal International*. DOI: 10.1111/j.1365-246X.2012.05663.x.
- Spada, G., Galassi, G., and Olivieri, M. (2014). “A study of the longest tide gauge sea-level record in Greenland (Nuuk/Godthab, 1958-2002)”. *Global and Planetary Change* 118, pp. 42–51. DOI: 10.1016/j.gloplacha.2014.04.001.

- Steger, C.R., Rijmer, C.H., and Broeke, M.R. van den (2017). “The modelled liquid water balance of the Greenland Ice Sheet”. *The Cryosphere* 11, pp. 2507–2526. DOI: 10.5194/tc-11-2507-2017.
- Steinberger, B. and Calderwood, A.R. (2006). “Models of large-scale viscous flow in the Earth’s mantle with constraints from mineral physics and surface observations”. *Geophysical Journal International* 167, pp. 1461–1481. DOI: 10.1111/j.1365-246X.2006.03131.x.
- Stibal, M., Box, J.E., Cameron, K.A., Langen, P.L., Yallop, M.L., Mottram, R.H., Khan, A.L., Molotch, N.P., Christmas, N.A.M., Cali Quaglia, F., Remias, D., Smeets, C.J.P.P., Broeke, M.R. van den, Ryan, J.C., Hubbard, A., Tranter, M., As, D. van, and Ahlstrom, A.P. (2017). “Algae Drive Enhanced Darkening of Bare Ice on the Greenland Ice Sheet”. *Geophysical Research Letters* 44. DOI: 10.1002/2017FL075958.
- Storms, J.E.A., Winter, I.L. de, Overeem, I., Drikkoningen, G.G., and Lykke-Andersen, H. (2012). “The Holocene sedimentary history of the Kangerlussuaq Fjord-valley fill, West Greenland”. *Quaternary Science Reviews* 35, pp. 29–50. DOI: 10.1016/j.quascirev.2011.12.014.
- Stroeve, J.C., Box, J.E., and Haran, T. (2006). “Evaluation of the MODIS (MOD10A1) daily snow albedo product over the Greenland ice sheet”. *Remote Sensing of Environment* 105, pp. 155–171. DOI: 10.1016/j.rse.2006.06.009.
- Stuhne, G. R. and Peltier, W.R. (2015). “Reconciling the ICE-6G\_C reconstruction of glacial chronology with ice sheet dynamics: The cases of Greenland and Antarctica: ICE-6G\_C and ICE-Sheet Dynamics”. *Journal of Geophysical Research: Earth Surface* 120.9, pp. 1841–1865. DOI: 10.1002/2015JF003580.
- Sutterley, Tyler C, Velicogna, Isabella, Csatho, Beata, Broeke, Michiel van den, Rezvan-Behbahani, Soroush, and Babonis, Greg (2014). “Evaluating Greenland glacial isostatic adjustment corrections using GRACE, altimetry and surface mass balance data”. *Environmental Research Letters* 9.1, p. 014004. DOI: 10.1088/1748-9326/9/1/014004.
- Tarasov, L., Dyke, A.S., Neal, R.M., and Peltier, W.R. (2012). “A data-calibrated distribution of deglacial chronologies for the North American ice complex from glaciological modeling”. *Earth and Planetary Science Letters* 315-316, pp. 30–40. DOI: 10.1016/j.epsl.2011.09.010.
- Tarasov, L. and Peltier, W.R. (2002). “Greenland glacial history and local geodynamic consequences”. *Geophysical Journal International* 150.1. DOI: 10.1046/j.1365-246X.2002.01702.x.
- Tarasov, L. and Peltier, W.R. (2003). “Greenland glacial history, borehole constraints, and Eemian extent”. *Journal of Geophysical Research: Solid Earth* 108. DOI: 10.1029/2001jb001731.
- Tedesco, M., Doherty, S., Fettweis, X., Alexander, P., Jeyaratnam, J., and Stroeve, J. (2016a). “The darkening of the Greenland ice sheet: trends, drivers, and projections (1981–2100)”. *The Cryosphere* 10, pp. 477–496. DOI: 10.5194/tc-10-477-2016.
- Tedesco, M., Mote, T., Fettweis, X., Hanna, E., Jeyaratnam, J., Booth, J.F., Datta, R., and Briggs, K. (2016b). “Arctic cut-off high drives the poleward shift of a new Greenland melting record”. *Nature Communications* 7. DOI: 10.1038/ncomms11723.

- Tedstone, A.J., Bamber, J.L., Cook, J.M., Williamson, C.J., Fettweis, X., Hodson, A.J., and Tranter, M. (2017). “Dark ice dynamics of the south-west Greenland Ice Sheet”. *The Cryosphere* 11, pp. 2491–2506. DOI: 10.5194/tc-11-2491-2017.
- Vermeersen, L.L.A. and Schotman, H.H.A. (2009). “Constraints on Glacial Isostatic Adjustment from GOCE and Sea Level Data”. *Pure and Applied Geophysics* 166, pp. 1261–1281. DOI: 10.1007/s00024-004-0503-3.
- Vermote, E. (2015). *MOD09A1 MODIS/Terra Surface Reflectance 8-Day L3 Global 500m SIN Grid V006. NASA EOSDIS Land Processes DAAC*. DOI: 10.5067/MODIS/MOD09A1.006.
- Wada, Y., Lo, M.H., Yeh, P.J.F., Reager, J.T., Famiglietti, J.S., Wu, R.J., and Tseng, Y.H. (2016). “Fate of water pumped from underground and contributions to sea-level rise”. *Nature Climate Change* 6, pp. 777–780. DOI: 10.1038/nclimate3001.
- Wake, L.M., Lecavalier, B.S., and Bevis, M. (2016). “Glacial Isostatic Adjustment (GIA) in Greenland: a Review”. *Current Climate Change Reports* 2.3, pp. 101–111. DOI: 10.1007/s40641-016-0040-z.
- Wang, S., Tedesco, M., Xu, M., and Alexander, P.M. (2018). “Mapping ice algal blooms in Southwest Greenland from space”. *Geophysical Research Letters* 45, pp. 11779–11788. DOI: 10.1029/2018GL080455.
- Weidick, A., Oerter, H., Reeh, N., Thomsen, H.H., and Thorning, L. (1990). “The recession of the Inland Ice margin during the Holocene climatic optimum in the Jakobshavn Isfjord area of West Greenland”. *Palaeogeography, Palaeoclimatology, Palaeoecology* 82.3-4, pp. 389–399. DOI: 10.1016/s0031-0182(12)80010-1.
- Whitehouse, P. (2018). “Glacial isostatic adjustment modelling: historical perspectives, recent advances, and future directions”. *Earth Surface Dynamics* 6, pp. 401–429. DOI: 10.5194/esurf-6-401-2018.
- Wientjes, I.G.M., Van De Wal, R.S.W., Schwikowski, M., Zapf, A., Fahrni, S., and Wacker, L. (2012). “Carbonaceous particles reveal that Late Holocene dust causes the dark region in the western ablation zone of the Greenland ice sheet”. *Journal of Glaciology* 58.210, pp. 787–794. DOI: 10.3189/2012JG11J165.
- Willemsse, N.W., Koster, E.A., Hoogakker, B., and Tatenhove, F.G.M. Van (2003). “A continuous record of Holocene eolian activity in West Greenland”. *Quaternary Research* 59.3, pp. 322–334. DOI: 10.1016/s0033-5894(03)00037-1.
- Williamson, C.J., Anesio, A.M., Cook, J., Tedstone, A., Poniecka, E., Holland, A., Fagan, D., Tranter, M., and Yallop, M.L. (2018). “Ice algal bloom development on the surface of the Greenland Ice Sheet”. *FEMS Microbiology Ecology* 94.3. DOI: 10.1093/femsec/fiy025.
- Williamson, C.J., Cook, J., Tedstone, A., Yallop, M.L., McCutcheon, J., Poniecka, E., Campbell, D., Irvine-Fynn, T., McQuaid, J., Tranter, M., Perkins, R., and Anesio, A. (2020). “Algal photophysiology drives darkening and melt of the Greenland Ice Sheet”. *Proceedings of the National Academy of Sciences* 117.11, pp. 5694–5705. DOI: 10.1073/pnas.1918412117.
- Wu, Z. and Huang, N.E. (2009). “Ensemble Empirical Mode Decomposition: A Noise-Assisted Data Analysis Method”. *Advances in Adaptive Data Analysis* 1.1, pp. 1–41. DOI: 10.1142/S1793536909000047.

- Yamauchi, H. and Takei, Y. (2016). “Polycrystal anelasticity at near-solidus temperatures”. *Journal of Geophysical Research: Solid Earth* 121.11, pp. 7790–7820. DOI: 10.1002/2016JB013316.
- Young, N.E. and Briner, J.P. (2015). “Holocene evolution of the western Greenland Ice Sheet: Assessing geophysical ice-sheet models with geological reconstructions of ice-margin change”. *Quaternary Science Reviews* 114, pp. 1–17. DOI: 10.1016/j.quascirev.2015.01.018.
- Zemp, M., Huss, M., Thibert, E., Eckert, N., McNabb, R., Huber, J., Barandun, M., Machguth, H., Nussbaumer, S.U., Gartner-Roer, I., Thomson, L., Paul, F., Maussion, F., Kutuzov, S., and Cogley, J.G. (2019). “Global glacier mass changes and their contributions to sea-level rise from 1961 to 2016”. *Nature* 568, pp. 382–386. DOI: 10.1038/s41586-019-1071-0.